Bioinspired conductive oriented nanofiber felt with efficient ROS clearance and anti-inflammation for inducing M2 macrophage polarization and accelerating spinal cord injury repair

Qingxia Zhang [a], Jiahe Zheng [a], Linlong Li [b], Jui-Ming Yeh [c], Xianrui Xie [a], Yuqing Zhao [a], Chengbo Li [a], Guige Hou [a], Huanhuan Yan [a,*]

[a] School of Pharmacy, The Key Laboratory of Prescription Effect and Clinical Evaluation of State Administration of Traditional Chinese Medicine of China, Binzhou Medical University, Yantai, 264003, PR China
[b] Key Laboratory of Polymer Ecomaterials, Changchun Institute of Applied Chemistry, Chinese Academy of Sciences, 5625 Renmin Street, Changchun, 130022, PR China
[c] Department of Chemistry and Center for Nanotechnology, Chung-Yuan Christian University (CYCU), Chung Li, 32023, Taiwan, Republic of China

ARTICLE INFO

ABSTRACT

Complete spinal cord injury (SCI) causes permanent locomotor, sensory and neurological dysfunctions. Targeting complex immunopathological microenvironment at SCI sites comprising inflammatory cytokines infiltration, oxidative stress and massive neuronal apoptosis, the conductive oriented nanofiber felt with efficient ROS clearance, anti-inflammatory effect and accelerating neural regeneration is constructed by step-growth addition polymerization and electrostatic spinning technique for SCI repair. The formation of innovative Fe^{3+}-PDA-PAT chelate in nanofiber felt enhances hydrophilic, antioxidant, antibacterial, hemostatic and binding factor capacities, thereby regulating immune microenvironment of SCI. With the capabilities of up-regulating COX5A and STAT6 expressions, down-regulating the expressions of IL1β, CD36, p-ERK, NFκB2 and NFκB signaling pathway proteins, the nanofiber felt attenuates oxidative stress injury, promotes M2 macrophage polarization and down-regulates inflammatory response. After implantation into complete transection SCI rats, the nanofiber felt is revealed to recruit endogenous NSCs, induce the differentiation of NSCs into neurons while inhibit astrocytes formation and inflammation, reduces glia scar, and promotes angiogenesis, remyelination and neurological functional recovery. Overall, this innovative strategy provides a facile immune regulatory system to inhibit inflammatory response and accelerate nerve regeneration after SCI, and its targeted proteins and mechanisms are first elucidated, which holds great application promise in clinical treatment of complete SCI.

1. Introduction

As a devastating disorder of the central nervous system, complete spinal cord injury (SCI) caused by acute mechanical force often results in permanent locomotor and sensory dysfunctions, which imposes ruinous impact on patients and heavy economic burdens to the society [1,2]. After primary spinal cord damage, decreased tissue pH caused by ischemic leads to acidic microenvironment [3]. Meanwhile, activated local inflammation contributes to excessive production of inflammatory cytokines, axonal inhibitory factors, and reactive oxygen species (ROS), ultimately causing severe oxidative stress, massive cell death, neuronal apoptosis, glial scar formation, and disruption and demyelination of axons at the lesion area [4,5]. In order to restore the damaged

neurological functions, clinical treatments of SCI comprise surgery, medication, cell therapy and physical stimulation, to promote axonal and neural regeneration, and reconstruct the damaged neural circuits [6]. However, therapeutic efficiency is limited owing to forming of a cascade of pathological events, including interruption of intercellular electrical signaling, neuroinflammation, inadequate neurotrophic factors, loss of neurons and glial scar formation at the damage site of SCI, accompanying the limited regenerative capability of spinal cord [7]. As a promising innovative therapeutic strategy for SCI, neural tissue engineering can promote nerve regeneration, drawing extensive attention of researchers [1,8,9]. Therefore, the construction of nerve implants with specific structures and functions that can fill the cystic cavity formed by the injury, rebuild neural electrical signal transmission of injury tissues,

accurately regulate macrophage polarization to M2 phenotype to reduce oxidative stress and attenuated inflammatory responses, meanwhile providing a platform for recruiting endogenous neural stem cells (NSCs) and differentiating into neurons, will break through the bottleneck of current complete SCI treatment.

As one of the crucial elements of neural tissue engineering, biomaterial scaffolds can provide mechanical support for the damaged tissues as well as be employed as carriers for delivering stem cells or bioactive factors to accelerate tissue regeneration [10,11]. The oriented nanofiber felt can provide topographical, biophysical, and biochemical cues to guide intrinsic neuron regeneration and neuron-axonal growth as well as regulate extrinsic microenvironment for facilitating SCI repair [12–14]. In addition, electrical signals are the basis of electrophysiology and neuroscience and play a crucial role in the nervous system [9,15]. Conductive polymer-based scaffolds, such as polyaniline, polypyrrole and polythiophene nanofiber felts, have attracted widespread attention in SCI repair field, owing to their reconstruction for neuronal communication and then realization of a natural integration of electronic and biological functions of spinal cord [16–18]. Among multiple conductive polymers, polyaniline is extensively used in nerve regeneration because of its easy synthesis, desirable solubility and electric conductivity [19]. More importantly, aniline oligomers with defined molecular structure can be cleared by renal metabolic pathways [20,21]. Meanwhile, they possess well electrical conductivity and electroactivity because of the unique conjugated structure and doping mechanism [9,22]. Therefore, conductive oriented nanofiber felt based on aniline oligomers can regulate the SCI microenvironment by simulating the high electric transmission capacity of the spinal cord and guiding cell outgrowth direction to reconstruct the signal transmission pathway and neuron differentiation of the injured nerve, thereby accelerating nerve regeneration. Previously, based on aniline tetramer and polycaprolactone (PCL), a micropatterned electrospun mesh with a regularly aligned valley and ridge structure has been prepared by rotation electrospinning technology [23]. The nanofiber mesh has guided the growth of NSCs and neurite along its valley, and regulated the differentiation of NSCs into neurons while suppressed the generation of astrocytes. However, due to the blending PCL and slight aniline tetramer-based polymer to form nanofiber mesh, it holds some drawbacks including poor flexibility, stretchability, conductivity and antioxidant capacity.

Furthermore, the hemostatic, antibacterial and antioxidant properties of biomaterials play an important role in facilitating SCI repair. Effective hemostasis at the injury site can prevent blood loss and related complications that may exacerbate the damage [24–26]. Y. Liang reported that Fe^{3+} doping can activate platelets and promote thrombus formation as well as endow biomaterial excellent antibacterial properties [27]. Meanwhile, the antibacterial property from Fe^{3+} doping can prevent infections which are common after SCI due to disrupted defense barriers [24,28,29]. In addition, phenolic compounds containing catechol are widely distributed in living organisms and involved in various biological functions. Mussel-inspired polydopamine (PDA) comprising rich catechol moiety is a promising antioxidant to reduce inflammation, alleviate oxidative stress and modulate immune microenvironment by scavenging ROS, down-regulating inflammatory mediators and up-regulating anti-inflammatory factors [30–32]. This dual action of reducing oxidative stress and regulating the immune response makes PDA a potentially valuable component in the development of treatments for spinal cord injury. Notably, phenolic and amine compounds can chelate Fe^{3+} to form a complex network structure, which can synergistically enhance the immunomodulation at the site of injury as well as improve the antimicrobial and hemostatic properties of biomaterials [24,33,34]. However, few studies have employed similar strategy to regulate the inflammatory microenvironment after complete SCI.

In addition to biomaterials, neurotrophic factors are essential in regulating the immune microenvironment of the spinal cord and endowing the biomaterials with neurogenic activity for the guidance of NSCs physiological activities [35–37]. The absence of endogenous NSCs

and neurotrophic factors after SCI hinders spinal cord tissue repair. Improved recruitment of endogenous NSCs is critical for functional recovery of SCI [38,39]. The chemokine stromal cell-derived factor-1a (SDF-1α) can efficiently recruit endogenous NSCs through the SDF-1α/CXC chemokine receptor 4 pathway, thereby further induce migration, proliferation and differentiation of NSCs [40]. Unfortunately, matrix metalloproteinases 2 and 9 (MMP2 and MMP9) activated after SCI may degrade SDF-1α and lead to neurodegeneration [41]. Meanwhile, recruited NSCs would more easily differentiate into glial cells rather than neurons *in vivo* ascribed to the adverse microenvironment after SCI [42]. Nerve growth factor (NGF) has the multiple biological effect of promoting the differentiation of endogenous NSCs into neurons, nourishing neurons as well as regulating axonal plasticity, neurotransmitter production and synaptic function, showing great regenerative potential in spinal cord injury repair [11,43,44]. Under pathological conditions caused by SCI, the depletion of local SDF-1α and NGF restricts the regeneration and repair of neural circuits seriously, indicating the necessity of continuous supply of SDF-1α and NGF in SCI repair. Therefore, integrating biological factors with biomaterials in a manner which is consistent with the pathological features of SCI will be the key to successfully restoring damaged function [1,45]. Studies had confirmed the a robust adhesion of PDA, which mainly stems from catechol and 5,6-dihydroxyindole (DHI) moieties through a delicate synergy of leading oxidation and subsidiary cyclization within its self-polymerization [22,32,46,47]. Accordingly, through governing mussel-inspired adhesion by self-polymerization of dopamine, SDF-1α and NGF can be efficiently and stably adhered to the surface of nanofiber felts, which then stimulate NSCs recruitment and promote NSCs differentiation to neurons and integration of the damaged spinal cord [48].
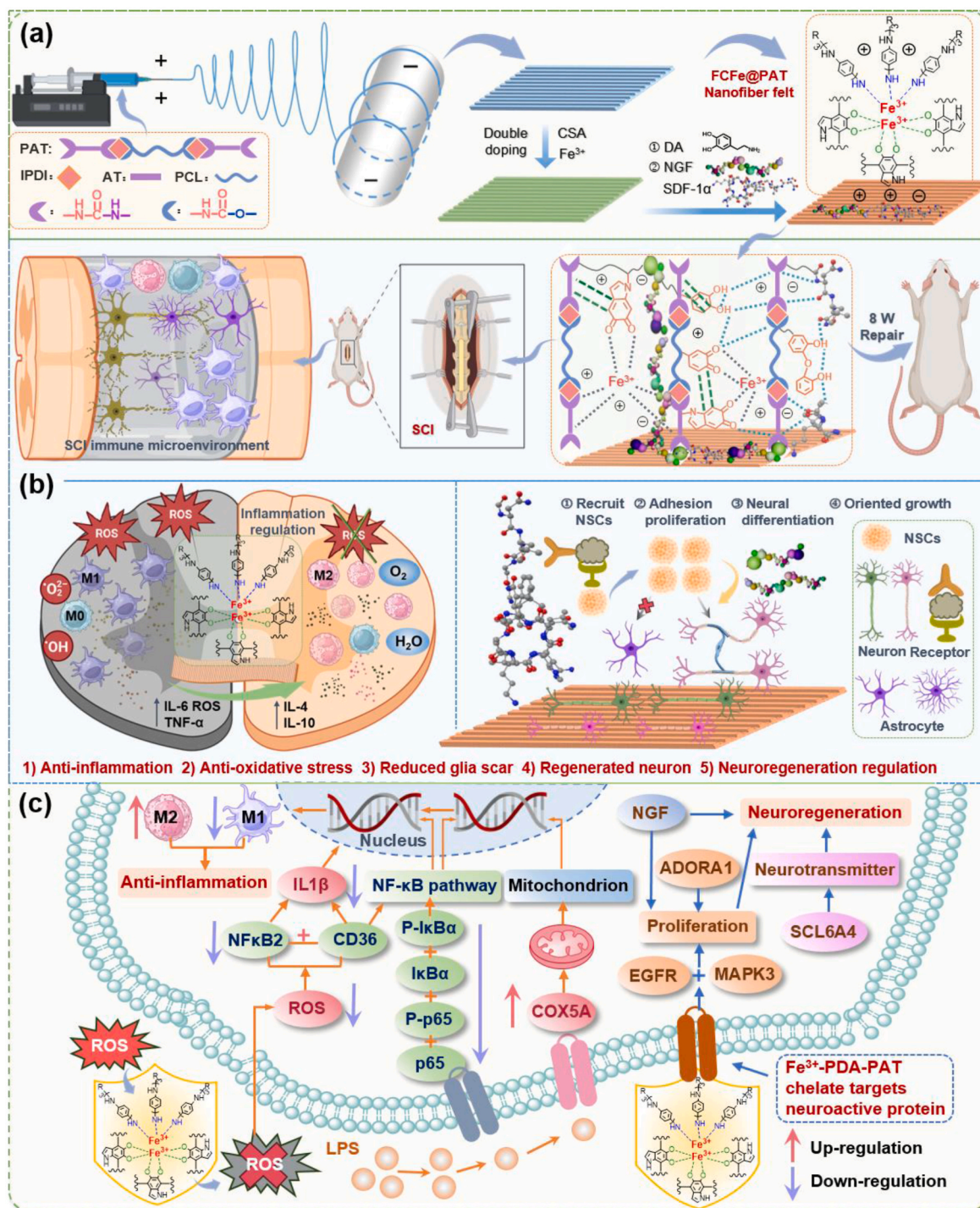
Herein, a bioinspired conductive oriented nanofiber felt with efficient intracellular ROS clearance function, anti-inflammatory activity and neurogenic potential was designed and fabricated to achieve inflammation suppression and neural regeneration for SCI repair (Scheme 1). A stretchable conductive polyurethane copolymer was synthesized by step-growth addition polymerization among amine-capped aniline trimer (AT), isophorone diisocyanate (IPDI) and PCL, and was further made into nanofiber felt with topography-guided cues by electrostatic spinning technique, and then doped with camphorsulphonic acid (CSA) and ferric chloride ($FeCl_3$) to enhance the electrical conductivity, antibacterial and hemostatic properties. Multiple hydrogen bond formation among IPDI units with AT and PCL units in a cooperative manner can significantly improve flexibility and stretchability of nanofiber felt. After that, PDA coating was deposited on the surface of the nanofiber felt accompanied by adhering NGF and SDF-1α to obtain immuno-microenvironment responsive antioxidant conductive nanofiber felt (FCFe@PAT). *In vitro* studies indicated that immunoregulatory FCFe@PAT nanofiber felt was conducive to recruitment, migration, extension and proliferation of NSCs and transmitting signal, and induced the differentiation of NSCs into neurons while inhibited astrocytes generation. A complete transection rat SCI model by removing 3 mm-long spinal cord at T9-T10 level was employed to evaluate the pro-regenerative efficacy, demonstrating its inhibited inflammatory function, accelerated nerve regeneration together with enhanced motor and functional recovery. Proteomics and molecular docking analysis were used to investigate the mechanism of anti-inflammatory and accelerating SCI repair of FCFe@PAT nanofiber felt. Therefore, this study provides a novel strategy for designing immuno-modulatory biomaterials to SCI repair and potent support for follow-up clinical application of bioinspired nanofiber felt.

2. Results and discussion

2.1. Preparation and physicochemical properties of PAT nanofiber felt

2.1.1. Primary selection of PAT

To prepare the bioinspired antioxidant conductive oriented

Scheme 1. Schematic illustration of the preparation and application of the bioinspired conductive oriented nanofiber felt (FCFe@PAT) for synergistic modulation of the immune microenvironment to accelerate spinal cord injury repair. **a)** Preparation of the FCFe@PAT nanofiber felt. **b)** The formation of multiple intermolecular and intramolecular forces on FCFe@PAT nanofiber felt, including hydrogen bonds, π- π interactions and coordinate bond, and its immune regulation for SCI repair by anti-inflammation, anti-oxidative stress, reduced glia scar, regenerated neuron and neuroregeneration regulation. **c)** Molecular mechanism of promoting M2 macrophage polarization and neuroregeneration by Fe^{3+}-PDA-PAT chelate in SCI repair.

nanofiber felt, PCL diols, AT and PAT with different AT content were synthesized [49]. PCL was obtained by ring-opening polymerization of ε-CL with initiator of BDO, and AT was synthesized by chemical oxidation with oxidant of ammonium sulfate. PAT was prepared by adding cyano groups in IPDI onto the reactive hydroxyl in PCL and amine in AT through nucleohilic addition reaction, respectively (Fig. S1, Supporting Information). The typical polymerization data including the number-average molecular weight and yield were summarized in Table 1. PAT10 with the M_n of 60.7 kDa, PDI of 1.95 and yield of 75 %, may be more suitable for preparing of nanofiber felt by electrospinning. Characterization via ^{1}H NMR and FT-IR showed that the PCL, AT and PAT with different AT content were successfully prepared (Fig. S2, Supporting Information). The details of results and discussion were available in **SI (1.7.1.)**.

Table 1
Molecular weight, PDI and yield of polymers with different aniline contents.

Polymer type	M_n (g mol^{-1})	M_w (g mol^{-1})	PDI	Yield (%)
PAT0	65256	78423	1.20	82 %
PAT5	43893	70869	1.61	79 %
PAT10	31162	60793	1.95	75 %
PAT15	12995	97838	7.52	65 %
PAT20	9999	57431	5.74	58 %

Then, the nanofiber felts of PAT with different AT content were prepared via rotary electrospinning. The microstructure of felts was investigated by SEM, which showed that nanofiber felt of PAT10 exhibited an oriented, smooth and uniform structure (Fig. 1a). In contrast, the structure of PAT15 and PAT20 were disordered, rougher and non-uniform, because of their poor dissolving ability in HFIP causing poor electrospinning ability. The average diameter of PCL, PAT0, PAT5, PAT10, PAT15 and PAT20 were 502.7 ± 74.89 nm, 576.13 ± 72.54 nm, 299.86 ± 71.71 nm, 398.86 ± 60.72 nm, 763.26 ± 142.41 nm and 711.62 ± 264.02 nm, respectively (Fig. 1b). Additionally, the length and direction of nanofiber felts were displayed in the wind rose diagram (Fig. 1c). The nanofibers in PAT0 and PAT10 groups presented long extensions in individual directions, while in the other groups were almost randomly stretched. Therefore, functional PAT10 presented the superior orientation, continuity and uniformity, which can guide neuronal cell oriented growth and neural tissue regeneration.

The thermal stability of nanofiber felts was analyzed by TGA and DSC (Fig. 1d and e) [48,50]. All the nanofiber felts showed the similar glass transition temperature (T_g) with the range of-14~16 °C, indicating their high elasticity similar to rubber at body temperature and maintain the flexibility of scaffold in SCI region. The melting point (T_m), $T_{95\%}$ and $T_{90\%}$ of PAT0 decreased compared with PCL, as the introduction of IPDI reduced the regularity and orderliness of the molecular chains in PCL [51–53]. The thermal stability of PAT increased compared to PAT0 due to the rigid benzene ring structure of AT. However, the regularity and orderliness of backbone in PAT were destroyed as the AT further increased, resulting the decrease of T_m, $T_{95\%}$ and $T_{90\%}$ after they reached a certain peak. In addition, the T_f gradually increased with the increase of AT. Nevertheless, PAT10 showed good thermal stability with T_m, $T_{95\%}$, $T_{90\%}$ and T_f of ≈59, 324.3, 329.2 and 770.1 °C (Fig. 1d and e), meeting the demand for thermal stability in SCI repair.

In order to evaluate their gains and losses of electron, electroactivity (or redox property) of PAT was investigated by testing the CV curves (Figs. 1f and 2b) [54]. Non-electroactivity presented in PCL and PAT0, and the nanofiber felts of PAT presented a pair of reversible redox peaks, which demonstrated their well electroactivity. The CV curves of PAT indicated that the oxidation potential increased while the reduction potential declined with increasing AT content, perhaps due to poor solubility of PAT with high AT content. The closed curve area of PAT10 was larger than that of other groups, and showed small variation after multi-segment cyclic scanning, revealing its superior redox property and charge−discharge capacity. The cationic agent was easily formed of PAT because of the excellent electroactivity, which can scavenge reactive oxygen and penetrate cytomembrane of bacteria and damage bacterial function. Thus, electroactive PAT10 may possess excellent antioxidant capacity and antibacterial activity.

The conductivity of polymers was generated by the electronic jumps within and between polymer chains, and the movement of anions or cations, which can be conducive to generating endogenous bioelectric signals in the body through the ion channel activity between adjacent cells, thereby achieving rapid intercellular communication including neurosignal transmission and neuron regeneration [9,23,55]. Resistances of the PCL and PAT0 were too high to be detected. As shown in Fig. 1g, the conductivity of PAT increased from 1.30 ± 0.23 × 10^{-6} to 4.18 ± 1.67 × 10^{-6} S m^{-1} with the increased AT content from 5 to 20 wt %. The low conductivity of PAT was due to the incorporation of nonconductive PCL and IPDI segments in the copolymer backbone. Such elevated conductivity of PAT may be ascribed to accelerate electron hopping and charge-carrier motion of AT, which formed more conductive microregions. Moreover, the conductivity of the CSA-doped PAT significantly increased ranging from 1.3 ± 0.38 × 10^{-5} to 3.66 ± 1.77 × 10^{-5} S m^{-1}, when increasing the AT content from 5 to 15 wt%. When the positive charge was injected into the AT chain during redox reaction, the negative charge can be incorporated to counterbalance the positive charge because of electroneutrality condition. Thus, the CSA doping can significantly improve the conductivity of PAT. In addition, oxidation state structure of AT can affect the electrical conductivity of PAT. AT in emeraldine base become conductive only through proton acid doping. Therefore, other organic acid such as toluene sulfonic acid (TSA) and dodecylbenzenesulfonic acid (DBSA) can be used to dope AT in order to enhance the conductivity of PAT. Besides, AT in leucoemeraldine or pernigraniline states can be doped by introducing K$^+$ or iodine to improve its conductivity. Notably, the conductivity of the CSA-doped PAT10 nanofiber felt closed to that of the amphibian motor nerve fiber myelin sheath about 10^{-4} S m^{-1} [20]. Therefore, CSA-doped PAT10 has a potential application in electrical signal sensitive neural tissue engineering.

The hydrophilicity of scaffold can efficiently impact biocompatibility and further inevitably affect SCI repair, and the water contact angles of copolymer and nanofiber felts were measured [56–58]. As shown in Fig. 1h and S3, PAT10 had a contact angle of 66.5 ± 0.89°, which can be classified as hydrophilic matter. Additionally, compared with co-polymers, the contact angle of PAT nanofiber felts obviously increased due to the oriented structure. The details of results and discussion were available in **SI (1.5.)**. Therefore, in order to maintain the ordered structures of nanofiber felt and possessed excellent physical and chemical properties, PAT10 nanofiber felt was selected to be doped by CSA, FeCl$_3$ and DOPA for subsequent experiments in order to achieve the best usage effect.

2.1.2. Element composition, mechanical performance, electroactivity and hydrophilicity of doped PAT10 nanofiber felts

The emeraldine base of AT segment in PAT was transformed into leucoemeraldine state on the basis of CSA doping. Afterwards, the trivalent iron ions (Fe^{3+}) and PDA deposited on nanofiber felts, and the terminal amino group in PAT10 and the phenolic hydroxyl group in PDA can chelate Fe^{3+} to form complex (or chelate) by the coordinate bond. The elemental composition of PAT10 and CFe@PAT was detected by EDX maps and quantitative analyses (Fig. 1i and j), where C (red), N (blue), and O (green) elements were uniformly distributed in the nanofiber felt. Simultaneously, S (yellow) and Fe (cyan) elements were detected in CFe@PAT with contents of 0.06 ± 0.04 % and 2.03 ± 0.2 %, respectively. In addition, UV–vis spectra of PAT10, CFe@PAT, and DCFe@PAT was detected as shown in Fig. 1k. DCFe@PAT exhibited UV absorption peaks of AT segment at 320 and 550 nm, Fe^{3+} at 200 nm and 245 nm, and PDA at 270 nm, confirming the successful doping of Fe^{3+} and adhesion of dopamine. Moreover, ICP results indicated molar ratio of doped Fe^{3+} and AT segments was about 1:3 in CFe@PAT (Fig. 1m). Doped PDA on nanofiber felt can chelate overloaded iron ions to form tris-complex of catecholate-iron according to previous research [24,33, 34,59]. Therefore, the coordination number of Fe^{3+}-PDA-PAT chelate was about 6 in DCFe@PAT (Fig. S6a, Supporting Information).

The excellent mechanical properties enabled biomaterials to be better adapted to SCI microenvironment [58,60]. Although the spinal cord is not a large-scale movement structure, it will inevitably undergo a certain degree of deformation in activities within living organisms. The flexibility and stretchability of nerve implants are essential for maintaining the function of the spinal cord and the overall coordinated operation of the body, which can dynamically respond to external stress and transfer external shocks. The tensile stress-strain curve, tensile force, tensile strength, Young's modulus and elongation at break of the nanofiber felts were shown in Fig. 2a. After introducing IPDI into PCL,
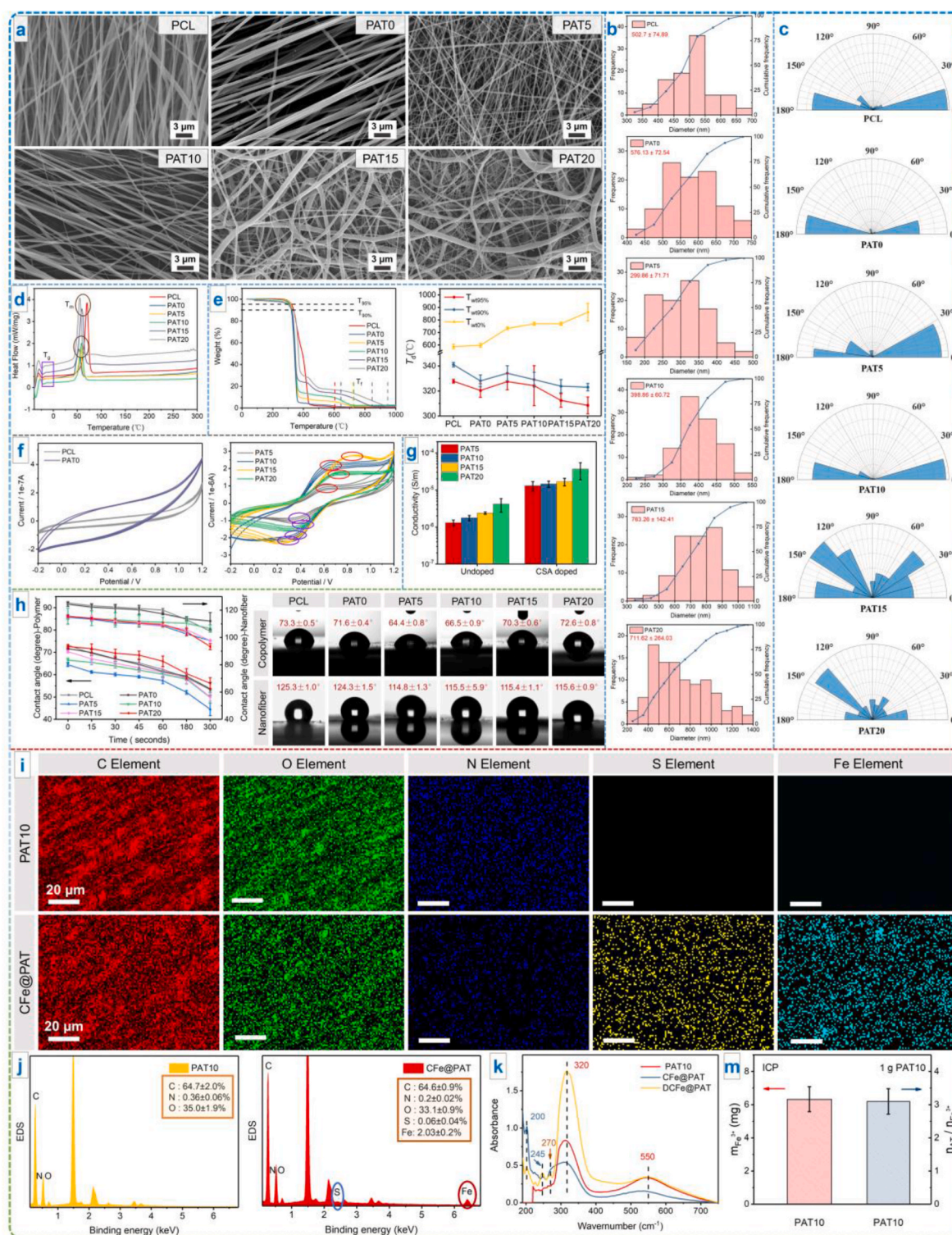
Fig. 1. Preparation and characterization of nanofiber felts. **a-g)** SEM images **a)**, frequency distribution **b)**, wind rose diagram (each blade represented the number of nanofibers within the corresponding angle range) **c)**, DSC curves **d)**, TGA curves and T_d **e)**, cyclic voltammetry curves **f)** and conductivities **g)** of nanofiber felts for different AT contents polymers. **h)** The variation of water contact angle and water droplets of both polymers and nanofiber felts within 5 min. **i-j)** EDX elemental mapping of C, O, N, S and Fe **(i)** and element content of PAT10 and CFe@PAT **j)**. **k)** UV–vis spectroscopy of PAT10, CFe@PAT and DCFe@PAT. **m)** ICP method for determining Fe^{3+} content and amount of substance ratio of doped Fe^{3+} and AT in 1g of CFe@PAT.

the tensile force, tensile strength, Young's modulus and elongation at break of PAT0 significantly improved, possibly due to the provision of more H bonds and physical crosslinking sites by IPDI. Notably, the elongation at break of PAT10 (432.6 ± 14.9 %) was significantly higher than that of PCL (61.3 ± 5.5 %) and PAT0 (102.9 ± 3.2 %). The high

stretchability of PAT10 can be attributed to the synergistic effect of intermolecular and intramolecular forces, and subsequent formation of multiple cross-linking mechanisms, including hydrogen bonds and electrostatic interaction (π – π conjugation and stacking interaction). However, PAT10 exhibited poor tensile force (1.36 ± 0.14 N), tensile
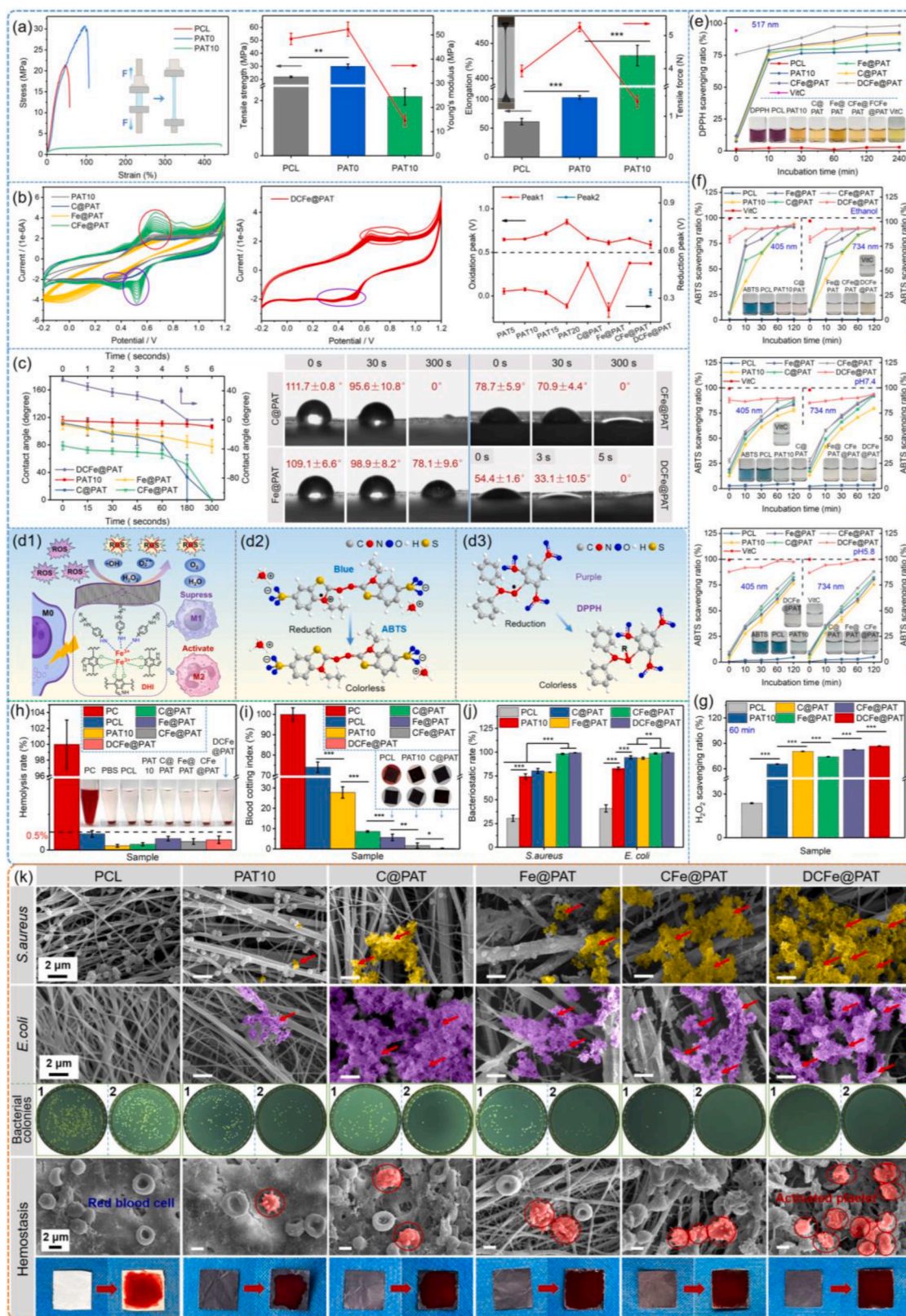
Fig. 2. Characterization of different nanofiber felts. **a)** Mechanical property. **b)** Cyclic voltammetry curve and oxidation and reduction peaks. **c)** The variation of water contact angle and water droplets within 5 min. **d)** The stick models for DPPH and ABTS clearance mechanisms. **e-g)** The scavenging ratio of DPPH **e)**, ABTS **f)** and H_2O_2 **g)** by nanofiber felts. **h)** Images of erythrocytes and hemolysis rate. **i)** Blood coagulation results containing images and blood clotting index (BCI). **j)** Bacteriostatic rate against *S. aureus* and *E. coli*. **k)** SEM images of fragmented *S. aureus* (yellow) and *E. coli* (purple), and colonies photographs of *S. aureus* (1) and *E. coli* (2), and SEM images of interaction of blood components with the felts. *$p < 0.05$, **$p < 0.01$, ***$p < 0.001$.

strength (2.15 $\pm$ 0.31 MPa) and Young's modulus (14.59 $\pm$ 2.1 MPa) compared to PAT0. This could be attributed to its weakened the crystallization ability owing to AT segment with steric hindrance disrupting the regularity of polymer backbone. Thereby the mobility and slip between the macromolecular chains were enhanced. Whereas the mechanical performance of PAT10 was sufficient to meet SCI repair requirements, because the Young's modulus and maximum failure stress of the human cervical spinal cord were 40.12 $\pm$ 6.90 and 62.26 $\pm$ 5.02 kPa, respectively [61,62]. Therefore, PAT10-based nerve implants can be adapted to SCI microenvironment.

Afterwards, the electroactivity of doped PAT nanofiber felts was further evaluated by testing CV curves (Fig. 2b) [63,64]. After multiple cyclic scanning, the nanofiber felts with CSA and Fe^{3+} doping all displayed a pair of reversible redox peaks in CV curves, demonstrating their excellent electroactivity. Notably, the reversible CV curves of DCFe@PAT showed two pairs of well-defined redox peaks of 0.59 $\pm$ 0.04 V/0.52 $\pm$ 0.007 V and 0.86 $\pm$ 0.006 V/0.34 $\pm$ 0.02 V, owing to the oxidizability-reducibility of PDA and AT. Furthermore, the closed areas of the CV curve of DCFe@PAT was much higher than that of other groups, revealing that its charge−discharge capacity was elevated. Moreover, the hydrophilicity of nanofiber felts was elevated by CSA and Fe^{3+} doping, and CFe@PAT exhibited a declined contact angle of 78.7 $\pm$ 5.9° at 0 s and 0° at 300 s (Fig. 2c and S3, Supporting Information). More importantly, DCFe@PAT with contact angle of 54.4 $\pm$ 1.6°at 0 S displayed superior hydrophilicity to other groups, and achieved a rapid water absorption capacity within approximately 5 s. Such elevated hydrophilicity could be attributed to formation of multiple mechanisms, including noncovalent interactions (hydrogen bonds), chelate (coordinate bonds), hydrophilic hydroxyl and carboxyl groups. Therefore, the nanofiber felt of DCFe@PAT with excellent hydrophilicity can facilitate NSCs adhesion and rapidly absorb internal exudate in SCI microenvironment.

2.2. Antioxidant activity by ROS and RNS scavenging capacity

2.2.1. ROS scavenging capacity

ROS can be generated through free radical oxidative stress in secondary injury after SCI. Excessive ROS in SCI area can bring about an increase in H^+ concentration, trigger an inflammatory response, cause NSCs damage, and inhibit nervous tissue regeneration [4,65–67]. The H_2O_2 scavenging ability was evaluated through the use of KI solution with an absorbance at 350 nm [4]. The H_2O_2 scavenging ratios and UV–vis spectrum were measured as displayed in Fig. 2g and S7. PAT10 presented better H_2O_2 scavenging ability than PCL, indicating the excellent antioxidant capacity of AT. The H_2O_2 scavenging ability of C@PAT and Fe@PAT was significantly higher than PAT10, and that of CFe@PAT was further elevated due to the combined effects of CSA and Fe^{3+}. More importantly, DCFe@PAT nanofiber felt presented a higher scavenging ratios than other groups. There was almost no absorbance at 350 nm for the DCFe@PAT, demonstrating that PDA coating improved the H_2O_2 scavenging capacity. The DHI structure formed by oxidation of dopamine exhibited high reactivity towards hydrogen peroxide radicals (HOO·), with the reaction between DHI and free radicals through the H atom transfer mechanism.

2.2.2. RNS scavenging ability

As depicted in Fig. 2d–f, S8 and S9, the RNS scavenging capacity of nanofiber felts was evaluated systematically through two typical nitrogen free radicals including 2,2-azino-bis(3-ethylbenzothiazoline-6-sulfonic acid) diammonium salt (ABTS) and 1,1-diphenyl-2-picrylhydrazyl (DPPH), and ascorbic acid (VitC) was used as a positive control [4,32,63,67].

ABTS is a stable RNS compound, and its ethanol and PBS solutions appear brilliant blue-green with a characteristic absorption peak at 405 and 734 nm. Except for dissolving in ethanol and pH 7.4 of PBS, ABTS was also scavenged in pH 5.8 of PBS to simulate the acidic

microenvironment of SCI. Compared to PCL, the absorbance peak decreased considerably upon treatments of PAT10 at 10 min, and further decreased in C@PAT and Fe@PAT groups, with evident fading, demonstrating an excellent RNS scavenging capacity. Moreover, CFe@PAT showed a higher $ABTS^{\bullet+}$ scavenging ratio than C@PAT and Fe@PAT, indicating that ABTS scavenging activity could be attributed to the joint effects of Fe^{3+} and CSA doping. PAT had oxidation-reduction activity, which could switch between the oxidized state, intermediate oxidized state and reduced state by different treatment. After CSA and Fe^{3+} doping, PAT was converted from the intermediate oxidized state to the reduced state, thus antioxidant activity was improved, which can be confirmed by aforementioned electrical activity results. Fig. 2f, S8b-6d and S9 also confirmed the time-dependent scavenging capacity of PAT and doped nanofiber felts. For instance, the $ABTS^{\bullet+}$ scavenging ratio (pH 7.4) increased from 27.0 $\pm$ 3.4 % to 93.4 $\pm$ 0.2 % for CFe@PAT as the time was increased from 0 min to 2 h. Notably, the peak disappeared after the reduction of DCFe@PAT accompanied by complete fading of solution at 0 min, which was similar to the results of VitC, indicating excellent $ABTS^{\bullet+}$ scavenging efficiency. However, the radical scavenging ratios of DCFe@PAT did not reach 100 %. Because the solutions of ABTS•+ appear pale yellow due to DOPA coating of nanofiber felt, which affected the absorbance value of the solution. The high antioxidant capacity of DCFe@PAT was ascribed to its superior redox property, which resulted in easily reducing $ABTS^{\bullet+}$ (Fig. 2d2). Thus, the $ABTS^{\bullet+}$ scavenging activity could be ascribed to the synergistic effects of doping of CSA and Fe^{3+} and PDA on PAT.

Another stable RNS, DPPH was used to investigate the anti-oxidation and anti-radical properties of different nanofiber felts, and its ethanol solution presents purple with a characteristic absorption peak at 517 nm to monitor its reduction process. As shown in Fig. 2e, S8a and S9, compared to PCL, a decreased absorption peak was observed at 517 nm after the treatment with PAT10, and DPPH solution appeared significant decolorization. When the DPPH solution was treated with doped PAT nanofiber felts, the DPPH scavenging ability was further improved. In addition, the characteristic absorption peaks of DPPH constantly decreased and DPPH scavenging ability gradually increased along with the time except for PCL group. Notably, as time increased from 0 min to 1 h, the DPPH scavenging ratio increased from 75.7 $\pm$ 0.08 % to 97.5 $\pm$ 0.06 % for DCFe@PAT, and the solution occurred complete color fading with no absorbance peak at 517 nm, indicating the DPPH radical was efficiently eliminated by DCFe@PAT (Fig. 2e). The DPPH results completely consistent with that of ABTS and the excellent DPPH scavenging activity of DCFe@PAT could be ascribed to the joint effects of AT, CSA/Fe^{3+} doping and PDA.

In summary, DCFe@PAT nanofiber felt with ROS and RNS scavenging capacities could be used as an excellent antioxidant agent to maintain the balance of the antioxidant defense system in SCI microenvironment, and efficiently inhibited oxidative stress response, and reduced inflammatory response through suppressing macrophage polarization towards M1 phenotype while activating its M2 phenotype (Fig. 2d1), and further played a neuroprotective role. Its function mechanism can be further explained by aforementioned redox results.

2.3. Antibacterial ability

SCI sites were easily infected by bacteria because of the inflammatory responses by secondary injury [68]. Thus, nanofiber felt with intrinsic efficient antibacterial ability was essential for SCI repair. The antibacterial activity of nanofiber felts against *S. aureus* and *E. coli* was evaluated through the plate-counting method and SEM observation [69, 70]. As shown in Fig. 2j and k, PCL presented inferior antibacterial activity with the bacteriostatic rate of below 41 %, and bacteria in PCL nanofiber felts appeared smooth and integral morphology. Whereas, *S. aureus* and *E. coli* displayed a significant decrease after the incubation with PAT10 for 18 h at 37 °C and partial bacterial structure collapsed, due to amino and benzene ring of AT damaging the fatty acids, proteins,

and peptidoglycans in the bacterial cell wall and membrane and then disrupting their function. In addition, antibacterial activity of doped PAT nanofiber felts was further enhanced, especially for CFe@PAT, bacteriostatic rate even reached 98.4 ± 0.6 % and 98.7 ± 0.7 % against *S. aureus* and *E. coli*, respectively. Most bacteria suffered serious rupture and were scavenged after the incubation with CFe@PAT for 18 h. This is due to the fact that Fe^{3+} can react with amino and sulfhydryl groups on intracellular proteins and bind to the active centers of proteins, thereby destroying the normal physiological structure of bacteria [28]. Besides, after the doping of CSA/Fe^{3+}, the emeraldine state of PAT transformed to the leucoemeraldine state, and then there are more amino and cationic groups, which leads to lysis and death of bacteria [71]. More importantly, after the introduction of PDA, DCFe@PAT can almost completely kill the bacteria with the bacteriostatic rate of 99.5 ± 0.1 % and 99.7 ± 0.5 % against S. aureus and E. coli, respectively. One aspect is that PDA can chelate metal ions on the bacterial surface, resulting in the rupture and shrinkage of bacteria, affecting the normal exchange of substances inside and outside the cells, and significantly influencing the survival of bacteria [72]. Another aspect is that the Fe^{3+}-PDA-PAT chelate formed by the chelation of the three substances has a synergistic effect, further enhancing the antibacterial activity. It not only destroys the cell membrane of microorganisms but also impacts the functions of intracellular enzyme activities, proteins and other biological macro-molecules. This multi-target attack approach makes it difficult for microorganisms to resist the antibacterial effect through a single defense mechanism.

These above results suggested that the DCFe@PAT had excellent antibacterial activity because of the synergistic effects of CSA/Fe^{3+} doping and PDA coating on PAT (Fig. 3c), which will effectively prevent bacterial infection in SCI repair process.

2.4. Blood compatibility evaluation

Blood clotting ability and hemostasis of the nanofiber felts were evaluated by *in vitro* whole blood-clotting assay and SEM observation, and a lower blood-clotting index (BCI) indicated a higher blood-clotting efficiency [24,48]. As depicted in Fig. 2i–k, after incubating the different nanofiber felts with blood for 5 min at 37 °C, most of the blood in PCL group was dispersed in the water, indicating its basic no coagulation. Additionally, BCI values of PAT (74.0 ± 2.6 %) were obviously lower than PCL (27.9 ± 2.8 %) ($p < 0.001$), and significantly decreased after CSA and Fe^{3+} doping of PAT10, with the BCI of below 10 %. After the PAT nanofiber felt doped with CSA/Fe^{3+}, blood intrinsic factors contact with abundant electric charge of CFe@PAT and may be activated, which may cause the formation of thrombin. It can promote platelet aggregation, release reactions, and stimulate platelet contractile proteins. The above function effect led to its improved coagulation. More importantly, DCFe@PAT presented BCI value of 0.25 %, which significantly lower than other groups, and the blood was completely rapidly absorbed by nanofiber felt, demonstrating its superior blood-clotting efficiency. Moreover, the nanofiber felt of DCFe@PAT could promote erythrocytes and platelets to aggregate at SCI area, then adsorb erythrocytes, effectively activate platelet and form a blood clot to accelerate the hemostasis, owing to porous nanofiber structure as well as inherent blood-clotting performance of Fe^{3+}/CSA doping and DOPA coating (Fig. 2k). The hemostatic mechanism of DCFe@PAT can be attributed to the activatied platelets, promoted platelet/erythrocyte adhesion and accelerated coagulation factor binding by Fe^{3+}-PDA-PAT chelate, and rapid absorption of exudate. Apart from that, abundant positive charges in chelate can efficiently bind with negative charges on hemocytes, which was beneficial for rapid hemostasis (Fig. 3a).

Excellent blood compatibility was indispensable for SCI repair [64, 73]. The blood compatibility of different nanofiber felts was further evaluated by *in vitro* hemolysis. After hatching in *in vitro* simulated physiological environment for 2 h, the appearance and color of erythrocytes contacting with different nanofiber felts and the

positive/negative control groups (Triton X-100/PBS) were observed and shown in Fig. 2h. All the nanofiber felts groups presented colorless appearance with consistency of PBS color, while the positive control group displayed bright red. Notably, the hemolysis rate of all the material groups was less than 0.5 %, which conformed international medical material standard, confirming that these nanofiber felts possessed excellent blood compatibility (Fig. 3b). Therefore, the DCFe@PAT nanofiber felt not only was non-toxic to blood cells, but also rapidly coagulate blood. The results demonstrated its appreciable application prospects for spinal cord injury repair.

2.5. In vitro biosafety evaluation

Biosafety is a prominent prerequisite for *in vivo* application of nanofiber felts [6,74]. Except hemolysis and coagulation tests, the cytotoxicity, live/dead cell staining, FITC/DAPI staining, SEM observation and CCK-8 assay were used to evaluate the cytocompatibility of nanofiber felts (Fig. S11 and **S12,** Supporting Information). The cytotoxicity was determined by culture of NIH3T3 cells with nanofibers extracts, followed by CCK-8 assay. As shown in Fig. S11a, the cell viability of all nanofiber felts was greater than 100 %, indicating no cytotoxicity. More importantly, CFe@PAT with cell viability of 145 ± 0.8 % significantly enhanced cellular activity compared to PCL and PAT10 ($p < 0.01$). Besides, the nanofiber felts did not show cytotoxicity and even promoted cell activity after twofold, fourfold, eightfold or sixteenfold dilution of the leachate.

Furthermore, the effects of different nanofiber felts on NIH3T3 cell adhesion and proliferation were evaluated by direct contact method. As shown in Fig. S11b, PAT10 exhibited higher cell viability than PCL after 12 h, 1 d, 3 d and 5 d of culture due to the cell promotion effects of AT, revealing the good biocompatibility of PAT10 nanofiber felt. In addition, the cell viability in CFe@PAT group was significantly higher than that in other groups ($p < 0.001$), demonstrating that CSA/Fe^{3+} doping improved the biocompatibility of PAT10. Moreover, NIH3T3 cells on CFe@PAT maintained the normal polygonal morphology, an elongated spindle-shaped appearance and more pseudopods for 12 h and 3 d (Fig. S12, Supporting Information), which orientationally aligned and extended along the fiber direction of the nanofiber felts. In addition, CFe@PAT nanofiber felt presented more live cells and less dead cells than PCL and PAT10 groups after 12 h and 3 d culture, proved by Live/Dead staining (Fig. S12, Supporting Information). The results confirmed that CFe@PAT can promote cell adhesion and proliferation and be safely used in SCI repair (Fig. S11c, Supporting Information). On the one hand, the conductivity of CFe@PAT can accelerate intra- and intercellular electrical signaling, thus promoting cell adhesion and proliferation. On the other hand, the rough porous structure and the increased hydrophilicity after CSA/Fe^{3+} doping of nanofiber felts can facilitate cell adhesion.

2.6. Intracellular ROS detection and immunomodulatory activity

Overproduction of reactive oxygen species (ROS) in SCI site can cause oxidative stress and cytotoxic inflammation, inducing extensive death of nerve cells at lesion sites [4,9]. To confirm the ability of biomaterials to scavenge intracellular excessive ROS in SCI microenvironment, 2,7-dichlorodihydrofluorescein diacetate (DCFH-DA) probe evaluated the intracellular antioxidant property in RAW 264.7 cells after culturing with different nanofiber felts (Fig. 4d and e). A strong green fluorescence signal was observed in the PCL group, demonstrating a high ROS content. However, the fluorescence intensity decreased in the PAT and CFe@PAT groups, due to the ROS scavenging ability of CSA/Fe^{3+} doping on PAT. More importantly, the DCFe@PAT group exhibited the lowest fluorescence intensity, which was mainly attributed to the excellent antioxidant property of Fe^{3+}-PDA-PAT chelate, which can completely scavenge ROS because of the combination of CSA/Fe^{3+} doping and PDA coating (Fig. 3d). Relative quantitative fluorescence
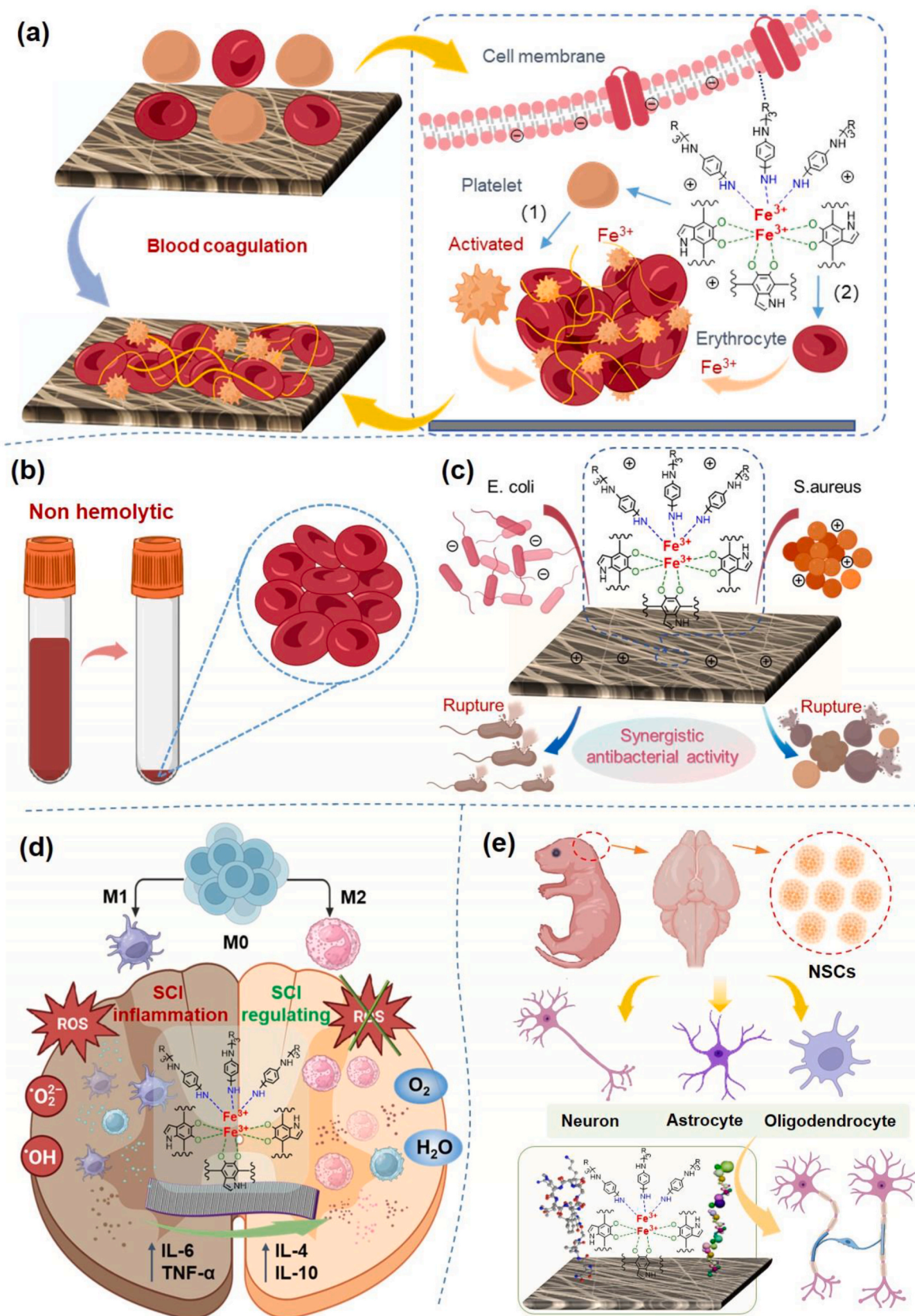
Fig. 3. a-e) Schematic diagram of blood coagulation **a)**, non-hemolysis **b)**, antibacterial activity **c)**, anti-inflammatory **d)** and promoting neuronal differentiation in NSCs mechanisms **e)** of nanofiber felt (FCFe@PAT).
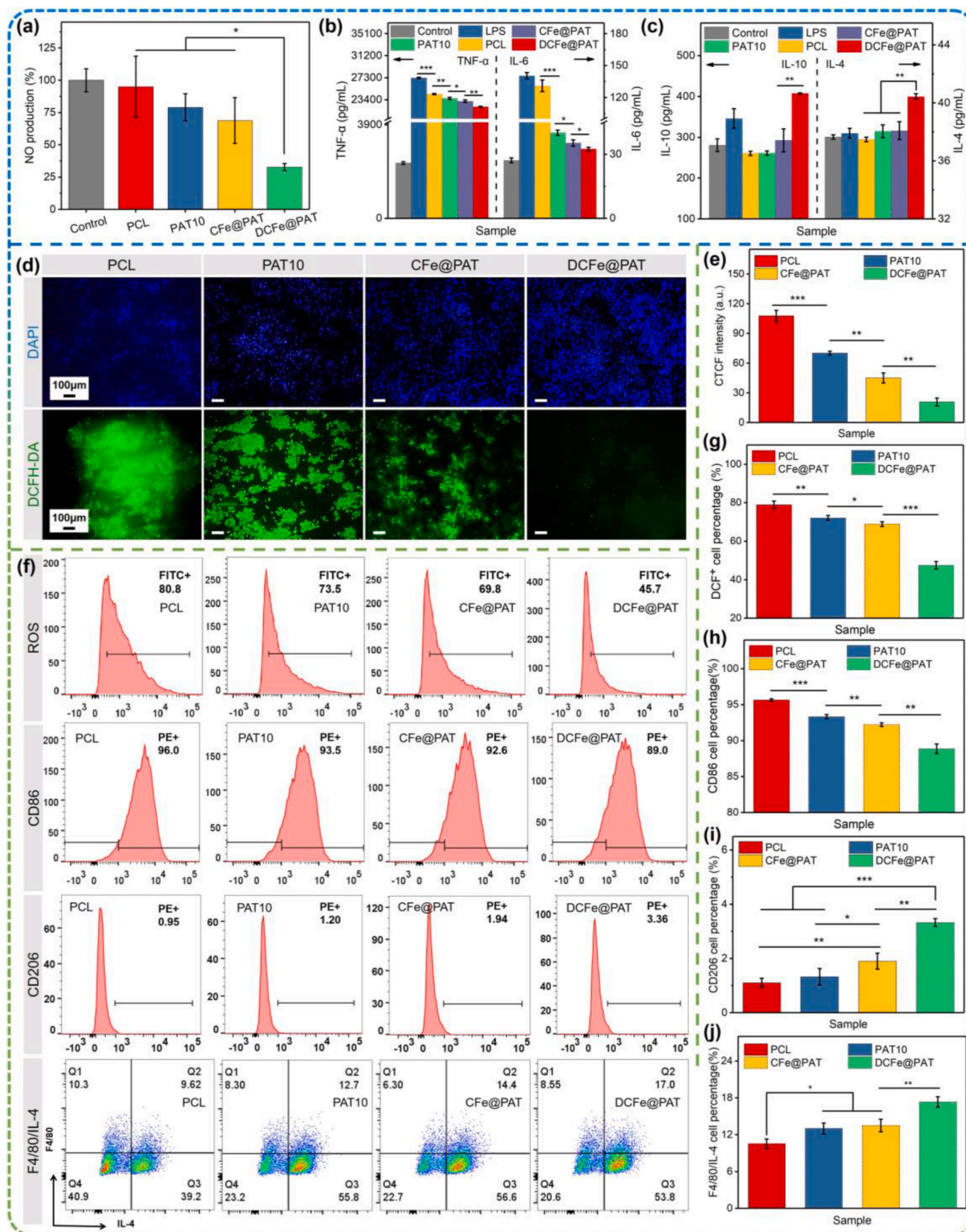
Fig. 4. In vitro immunomodulatory property of nanofiber felts on Raw 264.7 macrophages. **a-c)** NO production, and the expression levels of TNF-α, IL-6, IL-4, and IL-10 in cell supernatant after macrophages with LPS stimulation. **d)** Intracellular ROS scavenging performance evaluation DCFH-DA (green)/DAPI (blue) fluorescence staining. **e)** Quantitative statistics of average fluorescence intensity of DCFH-DA. **f)** ROS content analysis and polarization of macrophages were evaluated by expression of DCFH-DA (ROS, FITC-A), CD86 (M1, PE), CD206 (M2, PE), IL-4 (M2, FITC-A) and F4/80 (M0, PE) using flow cytometry. **g-j)** Quantitative statistics of DCF⁺, CD86, CD206 and F4/80/IL-4 cell percentage in flow cytometric analysis. *$p < 0.05$, **$p < 0.01$, ***$p < 0.001$.

results further confirmed prominent antioxidant performance of DCFe@PAT (Fig. 4e). The results of flow cytometry showed that the ROS positivity of PCL was 78.9 ± 1.9 %, and ROS scavenging efficacy was significantly increased for PAT10 with parallel DCF + cell percentage of 72.0 ± 1.3 % (Fig. 4f and g). In addition, the ROS clearance rate was further increased with CFe@PAT with the ROS positivity of 68.9 ± 1.2 %. Notably, the ROS positivity was markedly reduced to 47.5 ± 1.9 % in the DCFe@PAT group ($p < 0.001$), which was attributed to the presence of abundant reductive benzene ring, hydroxyl groups and amino-groups in the catechol groups and AT. These results demonstrated the effectiveness of the DCFe@PAT to reduce intracellular ROS production in macrophages and prevent cell injury from excessive amounts of ROS under oxidative stress.

Inflammation is associated with glial scar formation following SCI [75]. Macrophages can be divided into pro-inflammatory M1 phenotype and reparative M2 phenotype. Classically activated M1 macrophages, mainly induced by lipopolysaccharide (LPS), secrete high levels of inflammatory factors including nitric oxide (NO), interleukin-6 (IL-6) and tumor necrosis factor-α (TNF-α). Alternately activated M2 macrophages are mainly polarized by secreting anti-inflammatory cytokines of interleukin-4 (IL-4) and interleukin-10 (IL-10), which are indispensable in the repair process of SCI [67,76,77]. After measuring through Griess reagent method, NO production in DCFe@PAT was significantly decreased compared with other groups ($p < 0.05$) (Fig. 4a). After detecting by ELISA kits, LPS-induced RAW 264.7 macrophage secreted a large amount of TNF-α and IL-6, accompanied by little IL-10 and IL-4. However, after incubation with the PAT10 and CFe@PAT nanofiber felts for 24 h, the expression of the M1 macrophage marker gene TNF-α and IL-6 significantly decreased ($p < 0.001$), and the change of IL-4 expression level was not significant compared with the LPS stimulation group (Fig. 4b and c). Nevertheless, for DCFe@PAT nanofiber felt, the expression levels of TNF-α and IL-6 (surface markers for M1 phenotype) were significantly further reduced, together with the expression of IL-10 and IL-4 (M2 macrophage marker genes) were significantly elevated, confirming its excellent anti-inflammatory ability to inhibit M1macrophage activation and facilitate M1macrophage polarization due to the presence of PDA.

The transformation of macrophages promoted by DCFe@PAT in the cellular level was evaluated by flow cytometry [67,78]. As shown in Fig. 4f and h-j, after LPS stimulation, the percentages of CD86$^+$ (M1 phenotype), CD206+ (M2 phenotype) and F4/80/IL-4 macrophages were 95.7 ± 0.2 %, 1.11 ± 0.16 % and 10.5 ± 0.8 %, respectively. However, after PAT10 and CFePAT-based nanofibers treatment, the percentages of CD86$^+$ in M1 phenotype decreased to 93.3 ± 0.3 % and 92.2 ± 0.3 %, while CD206+ in M2 phenotype increased to 1.33 ± 0.30 % and 1.90 ± 0.29 %, and IL/4/F4/80 in M2 phenotype increased to 13 ± 0.9 % and 13.5 ± 1.0 %. More importantly, for DCFePAT group, the percentage of CD86$^+$ (88.8 ± 0.6 %) was significantly lower than that of other groups, while CD206+ (3.33 ± 0.14 %) and IL/4/F4/80 (17.3 ± 0.8 %) presented a completely contrary tendency. The results demonstrated that the nanofiber felt composed of Fe^{3+}-PDA-PAT chelate can effectively promote the transformation of RAW264.7 macrophages from the M1 into the M2 phenotype and consume the endogenous ROS thereby reducing the oxidative stress and inflammatory response, which could greatly promote SCI repair.

2.7. Cell recruitment, migration and proliferation

In addition to loss of immunoregulation, ROS oxidative stress and secretion of inflammatory factors, secondary complications after acute SCI also led to defects in NSCs and neurotrophic factors, neuron necrosis and formation of scar tissue, hindering SCI repair [1]. Therefore, ideal biomaterials should be able to recruit endogenous stem cells and induce neurons differentiation. Stromal cell-derived factor 1α (SDF1α) can interact with its specific receptor CXCR4 to induce the migration of progenitor cells and fibroblasts to the injury site [79,80]. Besides, NGF

promoted the differentiation of endogenous neural progenitor cells into neuron-like cells, and further nourished neurons and promoted axon growth [23,81,82]. Therefore, SDF-1α and NGF were adhered to DCFe@PAT nanofiber felt by bioadhesion of PDA, in order to confer neurogenic activity to nanofiber felt in the spinal cord microenvironment to guide NSCs differentiation. As shown in Fig. S13c, after incubation for 12 h, the SDF-1α and NGF adsorption percent on DCFePAT nanofiber felt were 95.7 ± 3.8 % and 99.9 ± 0.2 %, with the adsorption amount of 47.8 ± 1.9 ng and 99.9 ± 0.2 ng, respectively. The excellent growth factor adsorption capacity of DCFe@PAT nanofiber felt was attributed to high adhesion of DHI in PDA and rough fiber morphology. Subsequently, the SDF-1a and NGF release profiles were determined using ELISA kit within 168 h (Fig. S13a, S13b). Although the cumulative release percentages of growth factors were gradually increased with the extension of time, the final release of SDF-1α and NGF reached only 0.13 ± 0.002 % and 0.01 ± 0.001 %, demonstrating the excellent stability of growth factors on DCFe@PAT nanofiber felt, which was owing to high hydrophilicity and strong adhesion ability of PDA, and the formation of tight cross-linking structure between biomaterials and the growth factors.

NSCs isolated from the hippocampal region of the brain of SD rats within 12 h of the neonatal period were identified using bright field microscopy and immunofluorescence staining (Fig. 3e). All extracted cells were cultured and purified to suspend spherical cell clusters, which had positive Nestin expression and proved to be NSCs (Fig. S11d, Supporting Information).

For *in situ* SCI repair, cell recruitment and migration to the defect area is the critical first step [40,79]. Herein, transwell assay and cell scratch test were performed to verify the recruitment and migration ability of NSCs, BMSCs and HT22 cells by nanofiber felts (Fig. S11e, Supporting Information). As shown in Fig. S14a and S14c-d, in comparison with the PCL, PAT10 recruited slightly more BMSCs and NSCs, although the effectiveness was not significant. However, the Fe^{3+}-PDA-PAT chelate treatment resulted in improvement in the recruitment of BMSCs and NSCs. Additionally, SDF-1α/NGF-treated nanofiber felt significantly enhanced the recruitment of BMSCs and NSCs with the invasive cell numbers of 61.6 ± 0.3 % and 78.1 ± 2.5 %, respectively. The results of the scratch wound healing assay were shown in Figs. S14b-e. The migration rates were determined by quantitative analysis of the wound area at 0, 6, 12, and 24 h. FCFe@PAT group displayed the higher migration rate of HT22 cells at various time points than that of other groups, and change trend of migration ability in different groups was consistent with their recruitment effects. These results suggested that Fe^{3+}-PDA-PAT chelate exerted a positive impact on both recruitment effects of BMSCs and NSCs and migration capacity of HT22 cells, then SDF-1/NGF could effectively facilitate this trend.

Thereafter, the proliferation of NSCs was confirmed via CCK8 assays and SEM observation on days 3 and 7 post culture (Fig. S13, Supporting Information). A presence of Fe^{3+}-PDA-PAT chelate and SDF-1/NGF was significantly improved spherical cells (marked in red arrows) adhesion capacity on nanofiber felts. Besides, for FCFe@PAT group, more NSCs presented longer neurites and more extracellular matrix (ECM) secretion at 7d in comparison to 3d of culture, confirming that the NSCs adhered to nanofiber felt subsequent underwent early differentiation after proliferation. More importantly, the NSCs growth, neurite outgrowth and ECM secretion were showed along the nanofiber orientation, particularly, for DCFe@PAT and FCFe@PAT. The details of results and discussion were available in SI (1.8.5.). The results demonstrated that conductive oriented nanofiber felt coated with SDF-1 and NGF presented a synergistic positive effect on the adhesion, proliferation and neural differentiation of NSCs.

2.8. NSCs differentiation

NSCs was unable to maintain stemness and fast proliferation after 7 days of culture and underwent induced differentiation. Moreover, large

amount of axon growth inhibitors accumulated at SCI site, which further induce the differentiation of most NSCs toward astrocytes, resulting in glial scar formation, and the failure of neuronal and axonal regrowth. Therefore, to evaluate the neurogenic activity of nanofiber felts, immunofluorescence staining, western blotting and qRT-PCR were employed to detect the expression of neuron-specific markers in NSCs, including neurons (Tuj-1), astrocytes (GFAP) and F-actin, respectively. The seeded NSCs on FCFe@PAT nanofiber felt showed excellent typical neurogenic effect with exhibiting more neuron-like changes as indicated by synaptic morphology around cell bodies (blue arrows) (Fig. S13e, Supporting Information). The details of results and discussion were available in **SI** (**1.8.5.**). Immunostaining revealed that CSA/Fe^{3+} doping and PDA coating treatment on PAT increased both the fluorescent signal and proportion of neuron-specific class III beta-tubulin (Tuj-1) + neurons and F-actin, and decreased the proportion of glial fibrillary acidic protein (GFAP) + astrocytes with weak fluorescent signal compared to PAT and PCL (Fig. 5a and b and S16). It was noticeable that more Tuj-1+ neurons, more F-actin and fewer GFAP + astrocytes were generated in FCFe@PAT group compared with those in other groups. Semiquantitative analysis of fluorescent intensity also revealed significantly higher expression levels of Tuj-1+ and F-actin accompanied by lower expression level of GFAP+ in FCFe@PAT group (Fig. 5c). Additionally, the length of neurite outgrowth was also increased by the addition of CSA/Fe^{3+}, PDA and SDF-1α/NGF on PAT nanofiber felt (Fig. 5d and S15).

Western blotting (Fig. 5f) and band densitometry analysis (Fig. 5g) results also indicated that the Tuj-1 protein level of NSCs on FCFe@PAT group was markedly higher than that on other groups, meanwhile, GFAP protein level exhibited a completely opposite trend. The results confirmed that the doped PAT nanofiber felt and SDF-1α/NGF can synergetic up-regulated neuron protein expression while downregulated astrocyte expression. qRT-PCR was further carried out to evaluate the differentiation behavior of the NSCs at molecular level on nanofiber felts, which were highly consistent with immunofluorescence staining and western blotting results. As anticipated, FCFe@PAT significantly upregulated neuron gene expression while considerably decreased astrocyte gene expression, which further prove its neurogenic effect (Fig. 5e). These data suggested that FCFe@PAT efficiently induced neurogenesis and inhibited astroglial differentiation from NSCs (Fig. 3e). On the one hand, FCFe@PAT provided suitable electrical conductivity with appropriate surface hydrophilicity for facilitating intercellular electrical signaling transmission and NSCs adhesion. On the other hand, SDF-1α and NGF were responsible for the maintenance of multiple neurophysiological functions, which recruited endogenous NSCs while promoting their differentiation to neurons and inhibiting differentiation to astrocyte cells.

2.9. Functional recovery and safety assessment after SCI

The *in vivo* efficacy of nanofiber felts was evaluated by SD rat T9-T10 spinal cord complete transection model (Fig. 6a–h). After transection, nanofiber felts were transplanted into normal spinal cord tissues at both ends bridging the center of transection. SD rats were randomly divided into five treatment groups: control group, PCL, PAT10, CFe@PAT and FCFe@PAT. As shown in Fig. 6b1, there was a gradual reduction of visible cavity and scar tissue on SCI segments from the control group to the FCFe@PAT group at 8 weeks. The best repair result was presented in FCFe@PAT group, which displayed more newly regenerative tissue in the injury site. The recovery of hindlimb motor function after SCI was evaluated by Basso, Beattie, Bresnahan (BBB) score weekly after operation (Fig. 6c). All rats exhibited complete paralysis of hindlimbs immediately after surgery (BBB score = 0). The recovery of hindlimb motor function of rats in each group was in varied degrees. The rats in the PAT10 group presented a significant motor recovery compared to control group and PCL. Additionally, for CFe@PAT group, the rat paws landed on the ground with the BBB score of 8 at 8 weeks post-injury.

Notably, in comparison, superior recovery of motor function could be identified in FCFe@PAT group, as indicated by significantly higher BBB score than other groups at each time points from postinjury. At the eighth week, the BBB score of 10 was in FCFe@PAT group with weight-bearing clawed stepping. The locomotor recovery of rats at 8 weeks postinjury was assessed by the inclined plane test (IPT) (Fig. 6d), planar grid crawling experiment (Fig. 6e) and the inclined grid climbing test (Fig. 6b2). The maximum angle of IPT and the number of steps taken by rat hind limbs when its front limbs moved 100 steps in FCFe@PAT group were markedly higher than those of other groups, with the IPT angle value of 46.3 ± 2.4° and steps of 74 ± 6.1, consistent with the BBB score results, collectively demonstrating positive recovery for motor function. Very importantly, the rats in the FCFe@PAT group exhibited near normal hindlimbs recovery as indicated by both frequent plantar stepping and persistent dragging with weight-bearing (Fig. S17), meanwhile, occurred occasional coordination of forelimb-hindlimb during inclined grid climbing (Fig. 6b2). Furthermore, as a prominent indicator for the capacity of the locomotor signal conduction, MEP in rats of different groups was excited by electrophysiological test (Fig. 6f and g). The results showed that MEP amplitudes were significantly gradually increased following the order of rats in control, PCL, PAT10, CFe@PAT and FCFe@PAT groups. Notably, the waveforms of MEP in the left/right hindlimb of rats were partly recovered by implantation of FCFe@PAT nanofiber felt, which were the closest to those in the sham group. Collectively, the results indicated that FCFe@PAT nanofiber felt implantation could reduce the further damage risk of surviving motor neurons by effectively inhibiting scar regeneration and facilitating locomotor signal conduction after SCI, and then enable an amazing motor functional recovery.

The long-term biocompatibility evaluation of the nanofiber felts was conducted by *in vivo* subcutaneous implantation to investigate the toxicity to the main organs (heart, kidney, liver, lung, and spleen) of rats. After 8 weeks implantation, the main organs of the rats were collected and histologically evaluated. The cellular structures and morphologies of these organs in all the nanofiber felt groups was similar to that of control group in normal rat, showing no inflammatory infiltration or pathological changes in these organs (Fig. S18, Supporting Information). Therefore, all the nanofiber felts showed nontoxicity for various organs, indicating their good biocompatibility.

2.10. Immune regulation in SCI in vivo

A battery of inflammatory reactions was triggered in SCI lesion core, and the recruitment of macrophages and microglia reached the peak about 7 days after SCI [15,83]. So the inflammatory microenvironment in SCI site should be regulated by biomaterials for long-term nerve repair effect. Therefore, macrophages/microglia of M1-and M2-polarization were characterized by performing CD86 and CD163 immunofluorescence staining, respectively (Fig. 7b and c). It was extremely important that macrophage phenotypes transformed from pro-inflammatory M1 to anti-inflammatory M2 in SCI repair, while this transition was blocked after SCI. The results showed that CFe@PAT presented a significantly weakened fluorescence intensity of CD86 staining ($p < 0.001$) and a markedly enhanced fluorescence intensity of CD163 ($p < 0.001$) than those of control, PCL and PAT groups, owing to regulating macrophage polarization by CSA/Fe^{3+} doped PAT with antioxidant property. Notably, in comparison to other groups, FCFe@-PAT group displayed a significantly reduced proportion of M1 macrophages ($p < 0.05$), meanwhile a significantly raised percentage of M2 macrophages ($p < 0.05$), suggesting PDA coating and SDF-1α/NGF on nanofiber felt possessing anti-inflammatory function to secrete anti-inflammatory cytokines. The formed Fe^{3+}-PDA-PAT chelate and adhered SDF-1α/NGF synergistically resulted in enhancing cell-nanofiber felt interaction in SCI immune microenvironment, which could effectively polarize macrophages into the M2 phenotype to alleviate the local inflammatory response (Fig. 3d). Collectively, the
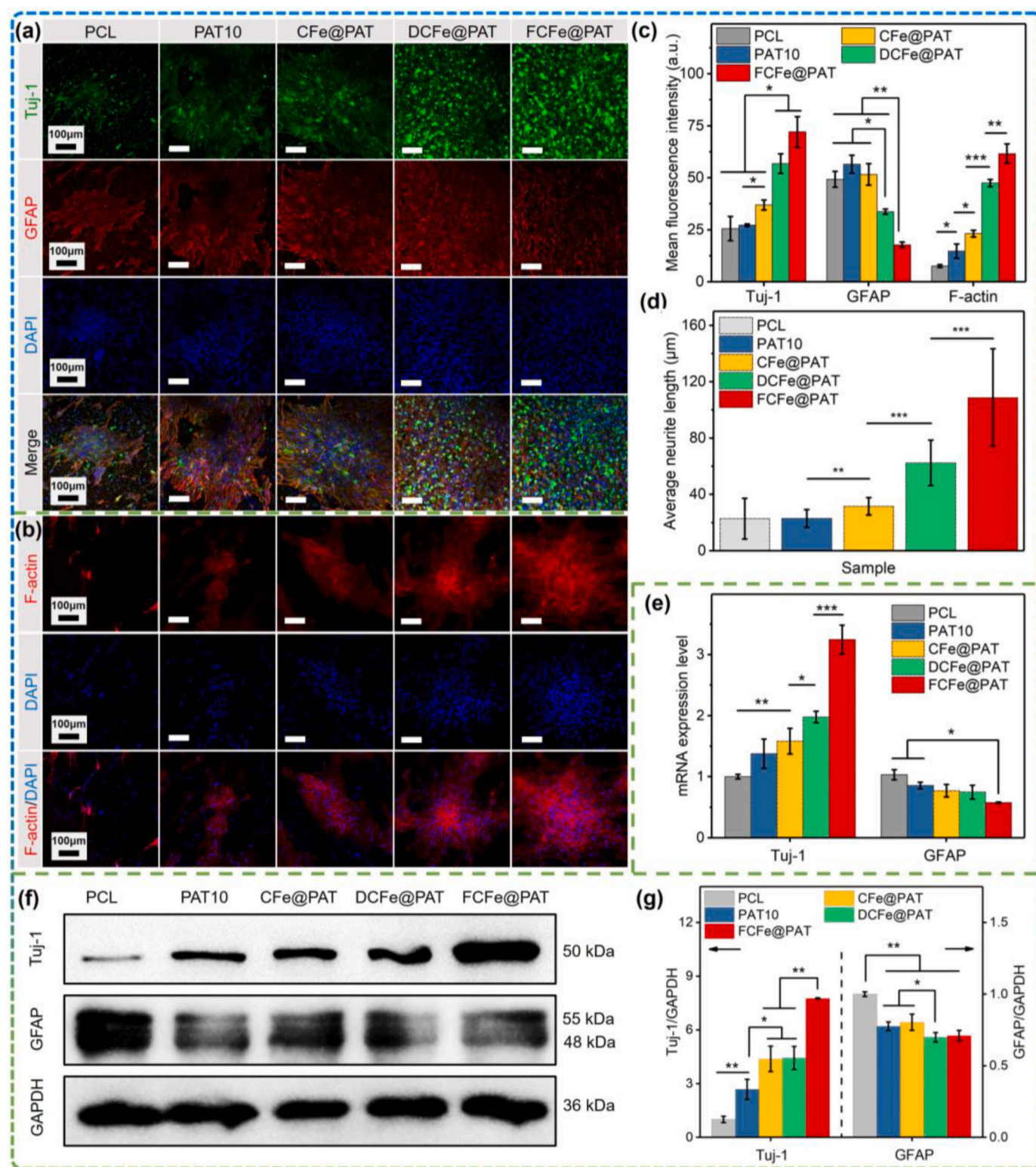
Fig. 5. Assessment of the differentiation of NSCs on nanofiber felts. **a-b)** Immunofluorescence staining for neurons (Tuj-1), astrocytes (GFAP), F-actin (phalloidin) and nucleus (DAPI) after 7 d cultivation of NSCs in differentiation medium. Characteristic images of each group at 200 (scale bar = 100 μm) magnification are shown. **c)** Quantitative statistics of average fluorescence intensity of Tuj-1, GFAP and F-actin. **d)** The length of neurite outgrowth detected in the Tuj-positive neurons. The mRNA expression level **e)** and western blotting for protein level detection **f)** of Tuj-1 and GFAP for 7 d. GAPDH was used as the internal control. **g)** Quantitative analysis of protein expression levels presented as a ratio between Tuj-1 and GFAP to GAPDH using ImageJ software. $*p < 0.05$, $**p < 0.01$, $***p < 0.001$.
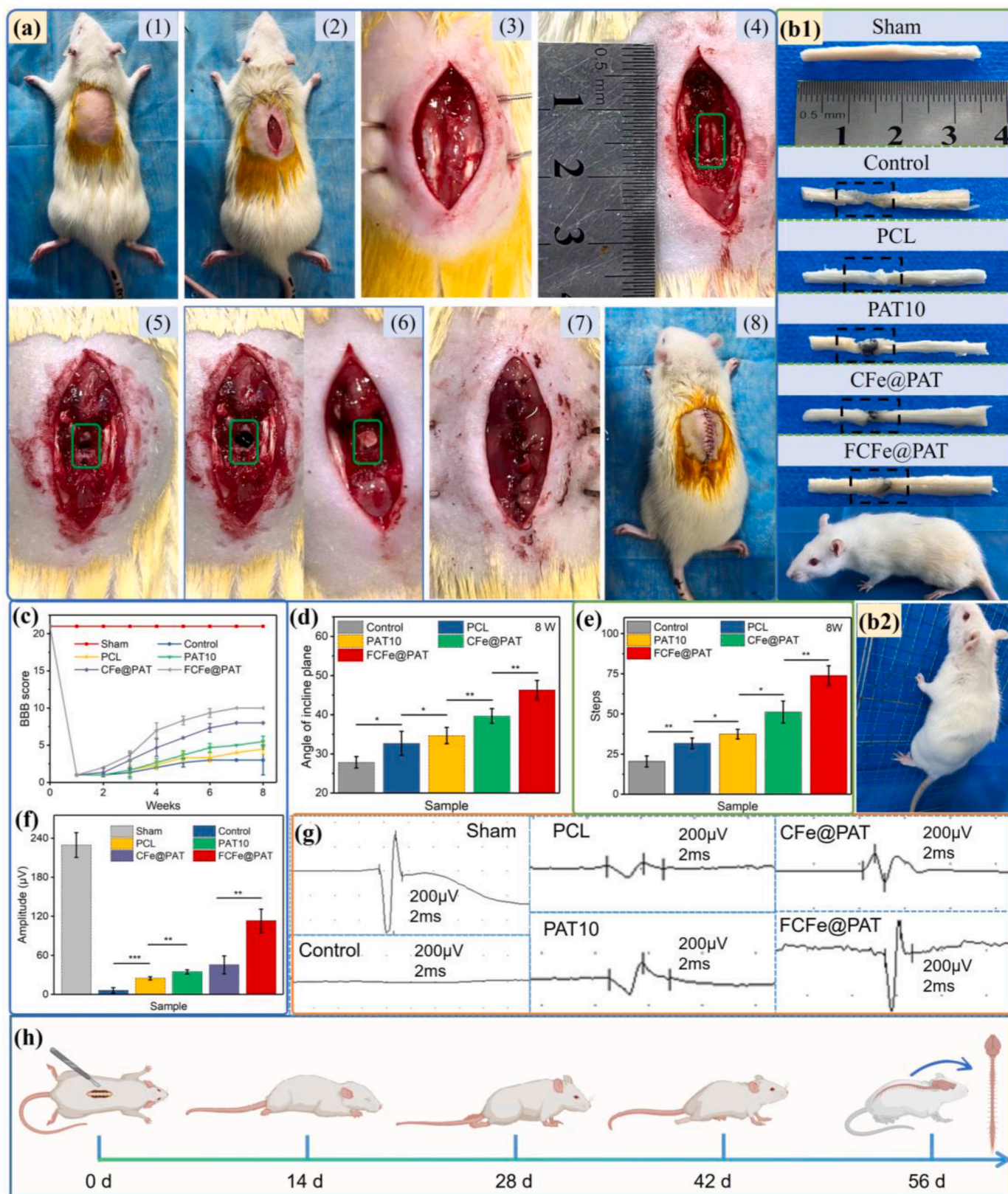
Fig. 6. Promotion effect of electrophysiological recovery and locomotor functional improvement in SCI model by nanofiber felts. **a)** Surgical procedures of spinal cord transection and nanofiber felts transplantation. 1–4: Exposure of T7–T10 spinal cord region; 5: Transection of T9–T10 spinal cord (3 mm); 6: Transplantation of nanofiber felts into the transection site. (7–8) Surgical suture. **b)** Images of rat's inclined grid climbing (1–5) and spinal cord samples (6) in different group at 8-weeks post-surgery.1-5 represented control group, nanofiber felts of PCL, PAT10, CFe@PAT and FCFe@PAT, respectively. **c)** BBB scores of hind limbs from different groups during the 8-week treatment. **d)** The maximum angle value of inclined plate when rat slid off it. **e)** The number of steps taken by rat hind limbs when its front limbs moved 100 steps on a horizontal grid in grid crawling experiment. **f-g)** Amplitude and MEP curves in different groups. **h)** Schematic diagram of motor function recovery in different stages of rat SCI. $*p < 0.05$, $**p < 0.01$, $***p < 0.001$.
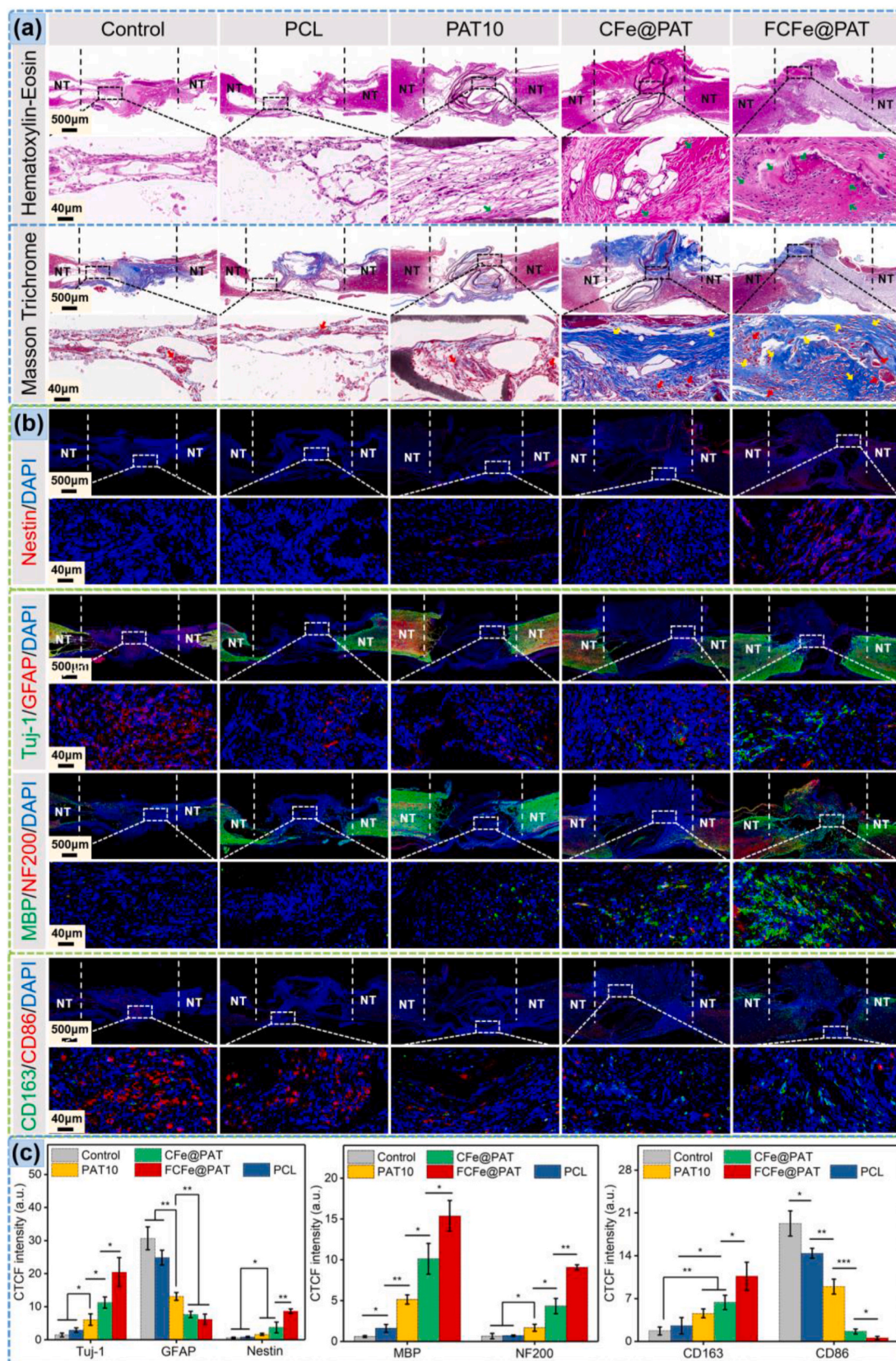
Fig. 7. Nerve regeneration regulation and inflammatory response after 8 weeks of SCI. **a)** HE and Masson staining images. Green (HE) and yellow (Masson) arrows represented new collagen tissue, and red arrows represented regenerated blood vessels. **b)** Immunofluorescence staining of nestin (green), Tuj-1 (green)/GFAP (red), MBP (green)/NF200 (red), CD163 (green)/CD68 (red) and DAPI (blue). The cross-sectional area of the spinal cord separated by dashed lines. **c)** Quantitative statistics of average fluorescence intensity of Nestin, Tuj-1, GFAP, MBP, NF200, CD68 and CD163. $*p < 0.05$, $**p < 0.01$ and $***p < 0.001$.

FCFe@PAT nanofiber felt presented excellent immunomodulatory effect by the synergistic response of Fe^{3+}-PDA-PAT chelate and SDF-1α/NGF to the inflammatory microenvironment of SCI, which facilitated pro-inflammation state of inflammation converting into anti-inflammation state, and motived injured tissue toward repair.

Subsequently, the inflammation of SCI site was evaluated by hematoxylin-eosin (HE) and Masson staining of spinal cord tissue sections at 4 and 8 weeks post-injury (Fig. 7a, S19). The injured segment tissue in the control group was disorganized with huge cavities inside, meanwhile, plentiful inflammatory cells and barely newly formed collagen appeared at 4 and 8 weeks. In contrast, the decreased area of the spinal cord cavity, reduced inflammation, increased amount of blood vessels (red arrows) and dense and abundant collagenous fibrous (green arrows in HE staining, yellow arrows in Masson staining) were presented in injured region after implantation of doped PAT nanofiber felt, especially for FCFe@PAT group. Meanwhile, the above effects were gradually enhanced from 4 to 8 weeks post-injury. The above phenomenon suggested that FCFe@PAT nanofiber felt can promote spinal cord tissue regeneration by reducing the inflammatory response as well as promoting angiogenesis and collagen deposition.

2.11. Nerve regeneration and remyelination

For repair of spinal cord complete transection injury, the replenishment of NSCs and neurons in the SCI lesion core was the foundation of neural circuit reconstruction [35,40]. To evaluate the NSCs migration capability and neuronal regeneration of the complete transected spinal cord after nanofiber felt implantation, nestin, neuronal class III β-tubulin (Tuj-1) and glial fibrillary acidic protein (GFAP) were immunostained to visualize migrated endogenous NSCs, new-born neurons and activated astrocytes at week 8 post-SCI, respectively (Fig. 7b and c). Following SCI, CFe@PAT nanofiber felt promoted endogenous NSCs migration to and accumulation around the injured region of rats, which was proved by enhancement of fluorescence intensity of nestin-positive. Notably, FCFe@PAT treatment presented the higher nestin fluorescence intensity in comparison with other groups, suggesting mediating endogenous NSCs migration by PDA and SDF-1α/NGF adhesions on PAT, which was consistent with *in vitro* cell results. Furthermore, control group displayed a large amount of activating astrocytes in lesion site and the formation of dense wall-like construct to isolating the adjacent host spinal cord. Then intensely GFAP-positive astrocytes formed glial scar boundaries and suppressed axon growth. Conversely, loosely arranged few astrocytes were appeared at the SCI lesion edge for connecting the host spinal cord and nanofiber felt in the CFe@PAT and FCFe@PAT groups, suggesting astrocytes being in a natural state rather than scar formation state due to the inhibition of M1 macrophage activation. Moreover, accompanied by a large amount of astrocytic scars, seldom Tuj1-positive neurons were existed in lesion site in control group, indicating the extremely limited neuronal regeneration ability without any treatment following SCI. In contrast, CFe@PAT showed plentiful regenerated Tuj-1-positive cells in the injury site, which was significantly higher than that of control, PCL and PAT groups ($p < 0.05$). Notably, in FCFe@PAT group, due to the recruitment and migration effects of PDA coating and SDF-1 α/NGF on NSCs, as well as further immunomodulation of macrophages and NSCs, the improved Tuj1-positive neurons regenerated into the lesion site with reduced astrocytes, compared to other groups ($p < 0.05$).

Then myelination of axons and regeneration of mature nerve fibers were evaluated by immunostaining for myelin basis protein (MBP) and neurofilaments 200 (NF200) at week 8 post-SCI, respectively (Fig. 7b and c). In the FCFe@PAT group, the abundant regenerated nerve fibers were consecutively sheathed with densely and organized myelin at the lesion edge and core, demonstrating its homogeneous and efficient regeneration capacities of nerve fibers and myelin sheaths. In comparison, such structures were sporadically observed in PAT10 and CFe@-PAT groups, and seldom appeared in control and PCL groups. Additionally, quantitative analysis indicated that MBP-positive and NF200- positive densities in FCFe@PAT group were significantly higher than those in other groups ($p < 0.05$). The results further confirmed that the transplantation of nanofiber felt to the injury site significantly promoted regeneration of nerve fibers and remyelination.

2.12. Immunomodulatory mechanism

To elucidate the immunomodulatory mechanism of the DCFe@PAT nanofiber felt, proteomics analyses were performed by culturing RAW 264.7 cells on various nanofiber felts [32]. The results revealed 4911 different proteins in each group. The volcano plots and heatmaps showed 82 significantly differentially expressed proteins (DEPs) between LPS group and DCFe@PAT group, with 65 up-regulated and 17 down-regulated DEPs (Fig. 8a and b). PAT10 group had 25 significantly altered proteins with 4 up-regulated and 21 down-regulated proteins, while CFe@PAT group with 0 up-regulated and 14 down-regulated proteins (Figs. S20b–e, Supporting Information), which revealed efficient inflammatory regulatory effect of PDA. Noteworthy, DCFe@PAT group significantly downregulated the protein expression of CD36, IL1β and NFκB2, and upregulated COX5A protein expression (Fig. 8a and b). Based on these differently expressed proteins, GO enrichment analysis were performed, composing of biological processes (BP), cellular components (CC), and molecular functions (MF) (Fig. 8d and S20a). The multiple inflammation related biological processes in DCFe@PAT, included RNS metabolic process, IL-6 production, canonical NF-κB signal transduction, tumor necrosis factor superfamily cytokine production, and production of molecular mediator involved in inflammatory response. In CC, DEPs were mainly enriched in myelin sheath, mitochondrial protein containing complex, oxyreducetase complex and outer membrane. The molecular functions mainly comprised oxyreducetase activity, acting on NADPH, immunoglobulin binding, and oxyreducetase activity, acting on paired donors, with incorporation or reduction of molecular oxygen. In addition, oxidative phosphorylation process of PAT and immune reaction process of CFe@PAT appeared in GO: BP analysis (Figs. S20f–g, Supporting Information). This confirmed that both PAT and doped PAT affected intracellular immune regulation, especially for PAT of PDA coating, significantly improved the cell defense against lipopolysaccharide induced oxidative stress, which proved its function mechanism of clearing intracellular ROS and inhibiting the expression of inflammatory cytokines TNF-α and IL-6. To further assess the underlying signal transduction pathways, KEGG pathway enrichment was performed (Fig. 8c), revealing the inflammatory regulatory effect of DCFe@PAT nanofiber felt achieved by influencing the inflammation related pathways, such as oxidative phosphorylation, pathways of neurogenesis, and neutrophil extracellular trapformation. On the basis of GO: BP results, DEPs enriched string plots displayed that the key differentially expressed proteins of IL1β and CD36 were screened to involve in the regulation of a variety of immune-related biological processes (Fig. 8e). Gene set enrichment analysis (GSEA) results also confirmed that DCFe@PAT participated in cell activation of regulation of immune response (Fig. 8f), which may correlate with the polarization of macrophages. The PPI network diagram showed that most proteins in the interactive network centered on UQCRC2/COX5A were distributed in mitochondria (Fig. 8g), combining with previous study [84–87], indicated that DCFe@PAT affected mitochondrial protein expression and alleviate mitochondrial dysfunction stimulated by LPS, thereby promoted M2 macrophage activation. More importantly, DCFe@PAT not only effectively down-regulated the protein expressions of IL1β, NFκB2 and CD36 and up-regulated COX5A protein expression (Fig. 8a and b), but also inhibited the NF-κB signal pathway-related proteins such as p65, P-p65, IκBα and P-IκBα (Fig. 8h and S21, Supporting Information), which were confirmed by Western blot analysis and quantitative analysis of protein expression levels. In addition, the downregulated IL1β expression presented in PAT10 and CFe@PAT groups (Figs. S20b–e, Supporting Information), meantime they also suppress the protein expressions of p65, P-p65, IκBαand P-IκBα (Fig. 8g).

Fig. 8. Anti-oxidative mechanisms of DCFe@PAT-treated LPS-induced inflammation. **a)** Volcano plots exhibiting the up or down-regulation DEPs in this mass spectrometry results. **b)** Heatmap analysis indicated 82 DEPs between the LPS and DCFe@PAT. **c)** Bubble charts of the KEGG enrichment analysis for DEPs. The x and y axes represent the enrich ratio and KEGG terms, respectively. **d)** Partial GO analysis of the DEPs. The x and y axes represent the number of genes and GO terms. BP, CC and MF represent biological processes, cellular composition and molecular function. **e)** Enriched chord diagram of the GO-BP analysis. **f)** GSEA analyses of the DEPs. **g)** PPI network analyses of the DEPs. Minimum required interaction score: 0.700. **h)** Western blot analysis of p65, P-p65, IκBα, and P-IκBα in RAW264.7 cells with different treatments.

Besides, CD36 and NFκB2 could interact with IL1β and regulate the NF-κB signal pathway (Fig. 8g) [32,88,89].

Additionally, Western blot was further conducted to identify the p-ERK and STAT6 signaling pathways for macrophage polarization effect of DCFe@PAT. As shown in Fig. S22, as a critical component of the MAPK signaling pathway, the phosphorylation of ERK (p-ERK), was significantly down-regulated upon DCFe@PAT treatment. Meanwhile, the expression level of the activator of transcription 6 (STAT6) was significantly increased after treating with DCFe@PAT nanofiber felt (Fig. S22, Supporting Information). Thereby, DCFe@PAT nanofiber felt could effectively prime macrophages toward to M2 phenotype by activate STAT6 signaling pathway (Fig. S23, Supporting Information). Collectively, the proteomics analysis revealed that doped PAT and PDA coating can collectively down-regulate CD36, p-ERK and NFκB2 expressions to down-regulate NF-κB signaling pathway and IL1β protein expression as well as up-regulate COX5A and STAT6 signaling pathway to effect mitochondrial protein expression for eliminating oxidative stress, promoting M2 macrophage polarization and inhibiting

inflammatory damage.

To evaluate the function mechanism of DCFe@PAT in human SCI, genes related to dopamine (437), aniline trimer (100) and SCI (7441) were obtained from the CTD, SwissTarget and GeneCards databases, respectively [90]. By intersecting genes of SCI with dopamine (DA) and aniline trimer (AT), the numbers of potential common genes associated with DA-SCI and AT-SCI were 393 and 88, respectively. Then the acquired potential co-genes were transferred to the STRING platform (https://string-db.org/) for PPI analysis and visualized in Cytoscape3.10.2 software, thereby interaction networks of DA-SCI and AT-SCI common genes were constructed respectively (Fig. S24a, Supporting Information). Based on these co-proteins, KEGG and GO analyses were performed. Pathways related to inflammatory response in SCI repair by DA include HIF-1 signaling pathway, cAMP signaling pathway, and TNF signaling pathway (Fig. S24e and **S24i,** Supporting Information). In addition, the regulation of immune system process and inflammatory response of DA presented in GO: BP analysis (Fig. S24b and **S24f,** Supporting Information). In GO: CC analysis, DEGs of DA were mainly
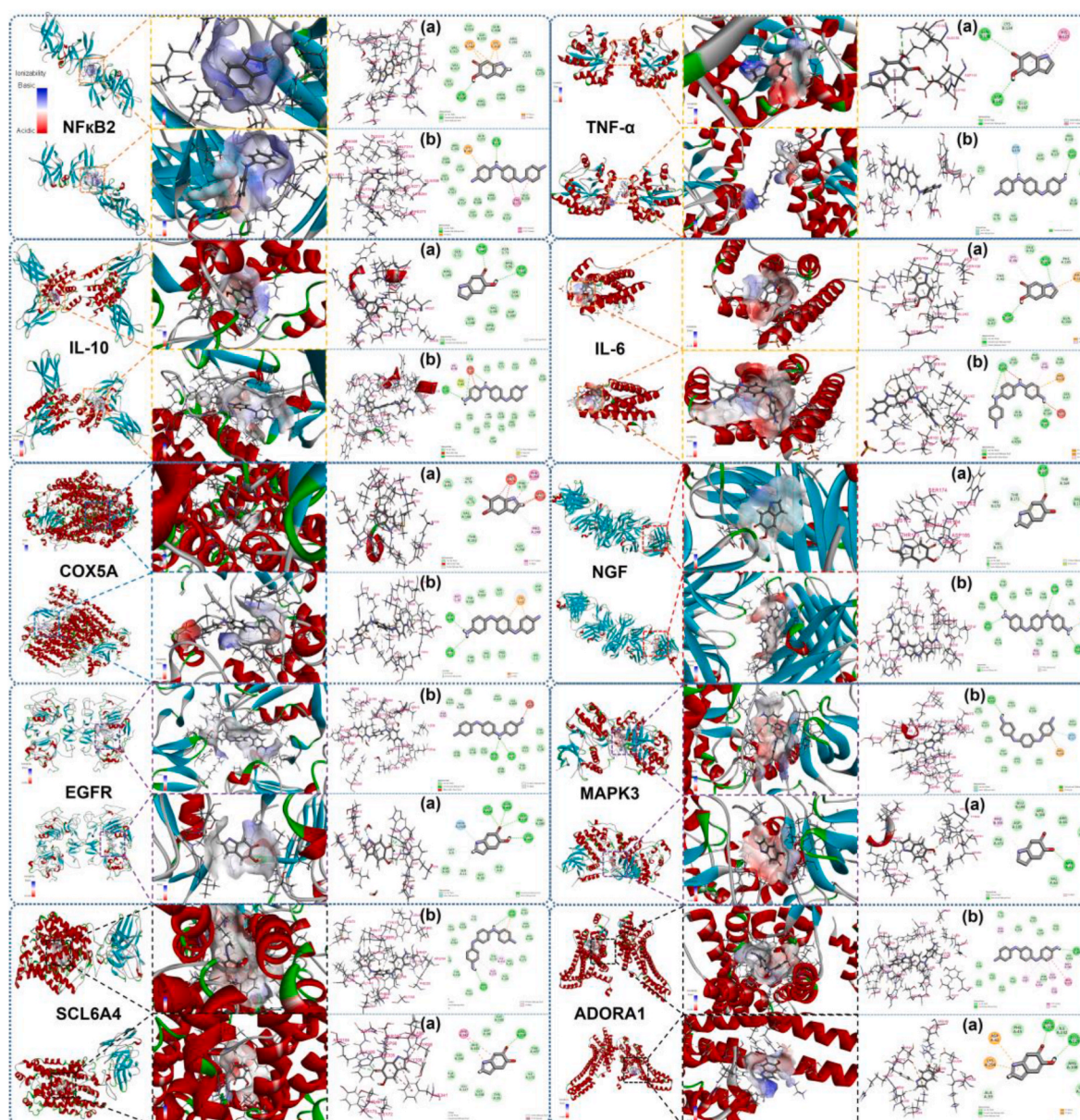

Fig. 9. Simulated 3D and 2D models of interaction between among different protein active sites (NFκB2, TNF-α, IL-10, IL-6, COX5A, NGF, EGFR, MAPK3, SCL6A4 and ADRA1) and DHI **a)** as well as AT **b)**.

enriched in mitochondrial matrix and membrane region (Fig. S24c and **S24h,** Supporting Information). In the result of GO: MF analysis, the large amounts of DEGs of DA in inflammation-related processes were enriched in oxidoreductase activity, catecholamine binding and adrenergic receptor activity (Fig. S24d and **S24g,** Supporting Information). Subsequently, the detailed KEGG annotation was presented (Fig. S24n, Supporting Information), indicating that AT had anti-inflammatory effects in SCI repair by targeting cAMP signaling pathway, Inflammatory mediator regulation of TRP channels and NF-κB signaling pathway. Moreover, GO enrichment analysis exhibited that several GO terms highly associated with inflammatory responses were augmented from the functional DEGs of AT, including "cellular response to nitrogen compound" in BP (Fig. S24j, Supporting Information), and "membrane raft" in CC (Fig. S24m, Supporting Information), and "oxidoreductase activity" in MF (Fig. S24k, Supporting Information). Therefore, DA and AT can target the human genes related to immune response in SCI repair, which further confirmed the results of proteomics analyses.

On the basis of lock-and-key principle of ligand-receptor interaction, molecular docking was a theoretical simulation method for computational predicting the binding mode and affinity between ligand molecule and its interacting receptor macromolecule [76]. To explore the association of DCFe@PAT with inflammatory signaling pathway-related proteins, the binding model and affinity of both AT and PDA made of catechol, dopamine quinone and DHI structures with inflammatory response-related receptors including IL1β, NFκB2, IL6, IL10, TNF-α and COX5A were visualized by molecular docking technique using Discovery Studio 2017R2 (Fig. 9, **S6b** and **S25,** Supporting Information). Among the ligands including catechol, dopamine quinone and DHI, the Hydroxyl, amino, benzene ring, and quinone ring of PDA ligands formed multiple interactions composing of typical hydrogen bonds, hydrogen bond, hydrohydrogen bond, carbon-hydrogen bond, pi-alkyl, pi-π interaction, pi-cation, electrostatic binding and salt bridge with the above six proteins around the active pocket. Notably, the binding energies of catechol with NFκB2, IL6, IL10 and TNF-α were 23.25, 41.26, 36.33 and 32.13 kcal mol^{-1}, which significantly higher than those on other ligands types in PDA (Table S1). In contrast, DHI presented lower binding energy with inflammation-related proteins, although it played a dominant role in PDA adhesion. In addition, amino, benzene ring and quinone ring in AT ligand could be reasonably embedded into the active pockets of NFκB2, IL6, IL10, TNF-α and COX5A proteins, meanwhile facilitated the formation of multiple interaction forces including hydrogen bond, hydrohydrogen bond, van der Waals force, π-π accumulation, πanion and πcation, between the small-molecule AT and the surrounding amino acid residues. Interestingly, compared to PDA, AT had lower binding energies with NFκB2 (14.60 kcal mol^{-1}), IL6 (27.72 kcal mol^{-1}), IL10 (−55.81 kcal mol^{-1}), TNF-α (18.11 kcal mol^{-1}) and IL1β (−57.62 kcal mol^{-1}), while presented the higher binding energy with COX5A (28.35 kcal mol^{-1}) (Table S1). In summary, catechol segment in Fe^{3+}-PDA-PAT chelate were responsible for the effective inhibition of inflammation by the DCFe@PAT nanofiber felt, due to the formation of abundant intermolecular binding forces with inflammatory related proteins. Additionally, AT could efficiently target mitochondria-related protein of COX5A to alleviate mitochondrial dysfunction, meanwhile inhibit the expression of NFκB signaling pathway proteins (p65, P-p65, IκBα and P-IκBα), causing its anti-inflammatory activity. Therefore, PDA and AT could synergistically regulate SCI immune microenvironment and promote SCI repair by inhibiting inflammatory response and reducing oxidative stress injury.

2.13. Neural regeneration mechanism

In order to investigate neural regeneration mechanism of DA and AT in SCI repair, PPI analysis and KEGG/GO gene enrichment analyses were performed (Fig. S24, Supporting Information), which involved some terms related to nerve and neurotransmitter delivery. In the results of DA-SCI co-genes KEGG, neural regeneration related pathways included neuroactive ligand-receptor interaction and dopaminergic synapse (Fig. S24e and **S24i,** Supporting Information). More importantly, large amounts of GO terms highly associated with neural regeneration were enriched from DA-SCI co-genes, including "modulation of chemical synaptic transmission" and "regulation of neuron apoptotic process" in BP (Fig. S24b and **S24f,** Supporting Information), and "dendrite", "axon", "postsynapse", "synaptic membrane", "neuronal dense core vesicle", "neuron part", and "neuron projection", etc. in CC (Fig. S24c and **S24h,** Supporting Information), and "neurotransmitter receptor activity", "neurotransmitter binding", "neurotransmitter receptor activity", "G protein-coupled amine receptor activity" and "G protein-coupled receptor binding" etc. in MF (Fig. S24d and **S24g,** Supporting Information). Additionally, in the results of AT-SCI co-genes KEGG (Fig. S24n, Supporting Information), the pathways related to neural network reconstruction in SCI repair included neuroactive ligand-receptor interaction, serotonergic synapse, dopaminergic synapse, neurodegeneration-multiple diseases and cholinergic synapse. GO analysis results showed plentiful enriched genes related to neuronal proliferation and differentiation as well as neurotransmitter conduction from AT-SCI co-genes, comprising "adenylate cyclase-modulating G protein-coupled receptor", "modulation of chemical synaptic transmission" and "adenylate cyclase-activating G protein-coupled receptor" in BP (Fig. S24j, Supporting Information), and "synaptic membrane", "G protein-coupled serotonin receptor complex", "glutamatergic synapse", "asymmetric synapse and "neuromuscular junction" in CC (Fig. S24m, Supporting Information), and "G protein-coupled amine receptor activity", "G protein-coupled peptide receptor activity", "dopamine neurotransmitter receptor activity", "protein-coupled acetylcholine receptor activity" and "G protein-coupled receptor binding" (Fig. S24k, Supporting Information) in MF.

Based on DA-SCI and AT-SCI PPI genes interaction network results (Fig. S24a, Supporting Information), molecular docking was performed to visualize binding models and affinity for the interaction between PDA/AT and the five neurorelated proteins including NGF, EGFR, MAPK3, SCL6A4 and ADORA1 (Fig. 9 and **S25,** Supporting Information). The ligands composed of AT, catechol, dopamine quinone and DHI formed multiple binding forces, including van der Waals force, conventional hydrogen bond, hydrohydrogen bond, carbon-hydrogen bond, π-alkyl, π-anion, π-cation, π-π accumulation and salt bridge with the amino acid residues of five protein receptors described above around the active pocket. Notably, binding energy between AT and three neurorelated proteins was the highest among the four ligands, with NGF of 35.94 kcal mol^{-1}, EGFR of 30.67 kcal mol^{-1} and ADORA1 of 36.69 kcal mol^{-1} (Table S1). Nevertheless, binding to the proteins of MAPK3 and SCL6A4 was significantly facilitated by a large number of interactions between the catechol ligand and the surrounding amino acids residues in the active site, with binding energies of 38.13 and 47.54 kcal mol^{-1}, respectively (Table S1). The above results confirmed that conductive AT and catechol of DCFe@PAT took a pivotal role in mediating the proliferation and differentiation of nerve cells, neuronal activity and transmission of neurotransmitters by targeting neurorelated proteins, thereby promoting nerve regeneration. Therefore, DCFe@PAT nanofiber felt could effectively regulate the binding model with proteins associated with neuronal proliferation, differentiation and neurotransmitter transmission, thereby promoted neuronal adhesion, proliferation, differentiation and axon extension, and accelerated the integration of injured spinal cord, and finally promoted SCI repair.

3. Conclusion

In this study, a bioinspired conductive oriented nanofiber felt was designed and fabricated by step-growth addition polymerization and electrostatic spinning technique for treatment of severely complete spinal cord injury. The formation of multiple hydrogen bond and conjugate interactions in nanofiber felt significantly improved its flexibility and stretchability. The CSA/FeCl$_3$ doping and PDA coating of PAT

formed Fe^{3+}-PDA-PAT chelate in DCFe@PAT, which enhanced the antioxidant capacity, hydrophily, electrical conductivity, electrical activity, antibacterial, hemostatic and binding factor capacities of the nanofiber felt. In addition, the Fe^{3+}-PDA-PAT chelate in DCFe@PAT nanofiber felt can regulate the inflammatory microenvironment by efficiently clearing intracellular ROS and promoting M2 macrophage polarization. Proteomic studies revealed AT and PDA in DCFe@PAT can jointly up-regulate the expressions of COX5A and STAT6 signaling pathway proteins to improve mitochondrial dysfunction, meanwhile down-regulate the expression of p-ERK, NFκB2 and CD36 to regulate NFκB signaling pathway and IL1β, which attenuated oxidative stress injury, and improve macrophage function and reduced inflammatory response. In addition, FCFe@PAT nanofiber felt not only facilitated endogenous NSCs recruitment, migration and proliferation, but also induced the differentiation of NSCs into neurons while inhibited astrocytes formation. *In vivo* complete transection rat SCI experiments confirmed that FCFe@PAT was conductive to inhibition inflammation, angiogenesis, nerve regeneration, remyelination and neurological functional recovery (hindlimb locomotor and electrophysiology function) in the SCI rats. These beneficial effects were attributed to the synergistic regulation of the inflammatory and the neural regeneration microenvironment by doped PAT and DA coating in Fe^{3+}-PDA-PAT chelate to accelerate the bridging of the injured spinal cord and SCI repair. In conclusion, this study first proposed that the potential functional proteins and mechanisms of AT and PDA in Fe^{3+}-PDA-PAT chelate in inhibiting inflammatory response and promoting nerve regeneration after SCI, and showed great promise in clinical application for SCI repair.

4. Experimental section

The detailed information could be found in supplementary file.

CRediT authorship contribution statement

Qingxia Zhang: Writing – original draft, Methodology, Investigation, Formal analysis, Data curation, Conceptualization. **Jiahe Zheng:** Validation, Resources, Investigation. **Linlong Li:** Writing – review & editing, Validation, Methodology. **Jui-Ming Yeh:** Writing – review & editing. **Xianrui Xie:** Visualization, Supervision. **Yuqing Zhao:** Supervision, Data curation. **Chengbo Li:** Supervision. **Guige Hou:** Project administration. **Huanhuan Yan:** Writing – review & editing, Visualization, Software, Project administration, Funding acquisition, Formal analysis, Conceptualization.

Ethics approval and consent to participate

All the animal experiments were approved by the Animal Ethics Committee of Binzhou Medical University and carried out by the "Guidelines for the Care and Use of Laboratory Animals of Binzhou Medical University".

Declaration of competing interest

The authors declare that they have no known competing financial interests or personal relationships that could have appeared to influence the work reported in this paper.

Acknowledgements

Appendix A. Supplementary data

Supplementary data to this article can be found online at https://doi.org/10.1016/j.bioactmat.2024.12.009.

References

[1] H. Shen, C. Fan, Z. You, Z. Xiao, Y. Zhao, J. Dai, Advances in biomaterial-based spinal cord injury repair, Adv. Funct. Mater. 32 (13) (2021) 2110628.

[2] Y. Fan, X. Wu, S. Han, Q. Zhang, Z. Sun, B. Chen, X. Xue, H. Zhang, Z. Chen, M. Yin, Z. Xiao, Y. Zhao, J. Dai, Single-cell analysis reveals region-heterogeneous responses in rhesus monkey spinal cord with complete injury, Nat. Commun. 14 (1) (2023) 4796.

[3] S. Wang, R. Wang, J. Chen, B. Yang, J. Shu, F. Cheng, Y. Tao, K. Shi, C. Wang, J. Wang, K. Xia, Y. Zhang, Q. Chen, C. Liang, J. Tang, F. Li, Controlled extracellular vesicles release from aminoguanidine nanoparticle-loaded polylysine hydrogel for synergistic treatment of spinal cord injury, J. Contr. Release 363 (2023) 27–42.

[4] Z. Li, T. Zhao, J. Ding, H. Gu, Q. Wang, Y. Wang, D. Zhang, C. Gao, A reactive oxygen species-responsive hydrogel encapsulated with bone marrow derived stem cells promotes repair and regeneration of spinal cord injury, Bioact. Mater. 19 (2023) 550–568.

[5] F. Kong, L. Yu, L. Gao, E. Xing, Y. Yu, X. Sun, W. Wang, D. Zhao, X. Li, Multifunctional hierarchical nanoplatform with anisotropic bimodal mesopores for effective neural circuit reconstruction after spinal cord injury, ACS Nano 18 (20) (2024) 13333–13345.

[6] B. Zhu, G. Gu, J. Ren, X. Song, J. Li, C. Wang, W. Zhang, Y. Huo, H. Wang, L. Jin, S. Feng, Z. Wei, Schwann cell-derived exosomes and methylprednisolone composite patch for spinal cord injury repair, ACS Nano 17 (22) (2023) 22928–22943.

[7] H. Liu, J. Yi, C. Zhang, Y. Li, Q. Wang, S. Wang, S. Dai, Z. Zheng, T. Jiang, P. Gao, A. Xue, Z. Huang, F. Kong, Y. Wang, B. He, X. Guo, Q. Li, J. Chen, G. Yin, S. Zhao, Macrophage GIT1 promotes oligodendrocyte precursor cell differentiation and remyelination after spinal cord injury, Glia 72 (9) (2024) 1674–1692.

[8] E.A. Kiyotake, M.D. Martin, M.S. Detamore, Regenerative rehabilitation with conductive biomaterials for spinal cord injury, Acta Biomater. 139 (2022) 43–64.

[9] Z. Liu, J. Lai, D. Kong, Y. Zhao, J. Zhao, J. Dai, M. Zhang, Advances in electroactive bioscaffolds for repairing spinal cord injury, Biomed. Mater. 19 (3) (2024) 032005.

[10] P. Song, T. Han, Z. Wu, H. Fang, Y. Liu, W. Ying, X. Wang, C. Shen, Transplantation of neural stem cells loaded in an IGF-1 bioactive supramolecular nanofiber hydrogel for the effective treatment of spinal cord injury, Adv. Sci. 11 (17) (2024) e2306577.

[11] K. Xi, Y. Gu, J. Tang, H. Chen, Y. Xu, L. Wu, F. Cai, L. Deng, H. Yang, Q. Shi, W. Cui, L. Chen, Microenvironment-responsive immunoregulatory electrospun fibers for promoting nerve function recovery, Nat. Commun. 11 (1) (2020) 4504.

[12] X. Dong, P. Wu, L. Yan, K. Liu, W. Wei, Q. Cheng, X. Liang, Y. Chen, H. Dai, Oriented nanofibrous P(MMD-co-LA)/Deferoxamine nerve scaffold facilitates peripheral nerve regeneration by regulating macrophage phenotype and revascularization, Biomaterials 280 (2022) 121288.

[13] J. Wang, H. Xiong, T. Zhu, Y. Liu, H. Pan, C. Fan, X. Zhao, W. Lu, Bioinspired multichannel nerve guidance conduit based on shape memory nanofibers for potential application in peripheral nerve repair, ACS Nano 14 (10) (2020) 12579–12595.

[14] S. Yao, Y. Yang, C. Li, K. Yang, X. Song, C. Li, Z. Cao, H. Zhao, X. Yu, X. Wang, L. N. Wang, Axon-like aligned conductive CNT/GelMA hydrogel fibers combined with electrical stimulation for spinal cord injury recovery, Bioact. Mater. 35 (2024) 534–548.

[15] M. Liu, W. Zhang, S. Han, D. Zhang, X. Zhou, X. Guo, H. Chen, H. Wang, L. Jin, S. Feng, Z. Wei, Multifunctional conductive and electrogenic hydrogel repaired spinal cord injury via immunoregulation and enhancement of neuronal differentiation, Adv. Mater. 36 (21) (2024) e2313672.

[16] S. Song, K.W. McConnell, D. Amores, A. Levinson, H. Vogel, M. Quarta, T.A. Rando, P.M. George, Electrical stimulation of human neural stem cells via conductive polymer nerve guides enhances peripheral nerve recovery, Biomaterials 275 (2021) 120982.

[17] C. Xu, P. Wu, K. Yang, C. Mu, B. Li, X. Li, Z. Wang, Z. Liu, X. Wang, Z. Luo, Multifunctional biodegradable conductive hydrogel regulating microenvironment for stem cell therapy enhances the nerve tissue repair, Small 20 (23) (2024) e2309793.

[18] B. Yang, C. Liang, D. Chen, F. Cheng, Y. Zhang, S. Wang, J. Shu, X. Huang, J. Wang, K. Xia, L. Ying, K. Shi, C. Wang, X. Wang, F. Li, Q. Zhao, Q. Chen, A conductive supramolecular hydrogel creates ideal endogenous niches to promote spinal cord injury repair, Bioact. Mater. 15 (2022) 103–119.

[19] E.N. Zare, P. Makvandi, B. Ashtari, F. Rossi, A. Motahari, G. Perale, Progress in conductive polyaniline-based nanocomposites for biomedical applications: a review, J. Med. Chem. 63 (1) (2020) 1–22.

[20] H. Liu, Y. Feng, S. Che, L. Guan, X. Yang, Y. Zhao, L. Fang, A.V. Zvyagin, Q. Lin, An electroconductive hydrogel scaffold with injectability and biodegradability to manipulate neural stem cells for enhancing spinal cord injury repair, Biomacromolecules 24 (1) (2023) 86–97.

[21] Y. Zhang, R. Zhang, Y. Tao, Conductive, water-retaining and knittable hydrogel fiber from xanthan gum and aniline tetramer modified-polysaccharide for strain and pressure sensors, Carbohydr. Polym. 321 (2023) 121300.

[22] H. Yan, L. Li, Z. Wang, Y. Wang, M. Guo, X. Shi, J.M. Yeh, P. Zhang, Mussel-inspired conducting copolymer with aniline tetramer as intelligent biological adhesive for bone tissue engineering, ACS Biomater. Sci. Eng. 6 (1) (2020) 634–646.

[23] H. Yan, Y. Wang, L. Li, X. Zhou, X. Shi, Y. Wei, P. Zhang, A micropatterned conductive electrospun nanofiber mesh combined with electrical stimulation for synergistically enhancing differentiation of rat neural stem cells, J. Mater. Chem. B 8 (13) (2020) 2673–2688.

[24] C. Lv, L. Li, Z. Jiao, H. Yan, Z. Wang, Z. Wu, M. Guo, Y. Wang, P. Zhang, Improved hemostatic effects by Fe3+ modified biomimetic PLLA cotton-like mat via sodium alginate grafted with dopamine, Bioact. Mater. 6 (8) (2021) 2346–2359.

[25] Y. Huang, C. Fan, Y. Liu, L. Yang, W. Hu, S. Liu, T. Wang, Z. Shu, B. Li, M. Xing, S. Yang, Nature-derived okra gel as strong hemostatic bioadhesive in human blood, liver, and heart trauma of rabbits and dogs, Adv. Healthcare Mater. 11 (18) (2022) e2200939.

[26] Z. Yang, L. Chen, J. Liu, H. Zhuang, W. Lin, C. Li, X. Zhao, Short peptide nanofiber biomaterials ameliorate local hemostatic capacity of surgical materials and intraoperative hemostatic applications in clinics, Adv. Mater. 35 (39) (2023) e2301849.

[27] Y. Liang, Z. Li, Y. Huang, R. Yu, B. Guo, Dual-Dynamic-bond cross-linked antibacterial adhesive hydrogel sealants with on-demand removability for post-wound-closure and infected wound healing, ACS Nano 15 (4) (2021) 7078–7093.

[28] Y. Lu, M. Zhao, Y. Peng, S. He, X. Zhu, C. Hu, G. Xia, T. Zuo, X. Zhang, Y. Yun, W. Zhang, X. Shen, A physicochemical double-cross-linked gelatin hydrogel with enhanced antibacterial and anti-inflammatory capabilities for improving wound healing, J. Nanobiotechnol. 20 (1) (2022) 426.

[29] L. Qiao, Y. Liang, J. Chen, Y. Huang, S.A. Alsareii, A.M. Alamri, F.A. Harraz, B. Guo, Antibacterial conductive self-healing hydrogel wound dressing with dual dynamic bonds promotes infected wound healing, Bioact. Mater. 30 (2023) 129–141.

[30] Q.S. Deng, Y. Gao, B.Y. Rui, X.R. Li, P.L. Liu, Z.Y. Han, Z.Y. Wei, C.R. Zhang, F. Wang, H. Dawes, T.H. Zhu, S.C. Tao, S.C. Guo, Double-network hydrogel enhanced by SS31-loaded mesoporous polydopamine nanoparticles: symphonic collaboration of near-infrared photothermal antibacterial effect and mitochondrial maintenance for full-thickness wound healing in diabetes mellitus, Bioact. Mater. 27 (2023) 409–428.

[31] W. Ma, X. Zhang, Y. Liu, L. Fan, J. Gan, W. Liu, Y. Zhao, L. Sun, Polydopamine decorated microneedles with Fe-MSC-Derived nanovesicles encapsulation for wound healing, Adv. Sci. 9 (13) (2022) e2103317.

[32] K. Wang, W. Mao, X. Song, W. Feng, G. Wang, T. Zhang, T. Xu, M. Chen, Y. Chen, B. Peng, Composition-reinforced polydopamine nanoenzyme for improved impairment of prostatitis-damaged sexual behavior and enhanced anti-prostate cancer, Adv. Funct. Mater. 34 (19) (2024) 2313528.

[33] H. Geng, Z. Li, Z. Li, Y. Zhang, Z. Gao, L. Sun, X. Li, J. Cui, S. Ni, J. Hao, Restoring neuronal iron homeostasis revitalizes neurogenesis after spinal cord injury, Proc. Natl. Acad. Sci. U.S.A. 120 (46) (2023) e2220300120.

[34] N. Abie, C. Ünlü, A.R. Pinho, M.C. Gomes, T. Remmler, M. Herb, D. Grumme, E. Tabesh, M.A. Shahbazi, S. Mathur, J.F. Mano, H. Maleki, Designing of a multifunctional 3D-printed biomimetic theragenerative aerogel scaffold via mussel-inspired chemistry: bioactive glass nanofiber-incorporated self-assembled silk fibroin with antibacterial, antiosteosarcoma, and osteoinductive properties, ACS Appl. Mater. Interfaces 16 (18) (2024) 22809–22827.

[35] W. Zhang, M. Liu, J. Ren, S. Han, X. Zhou, D. Zhang, X. Guo, H. Feng, L. Ye, S. Feng, X. Song, L. Jin, Z. Wei, Magnetic nanoparticles and methylprednisolone based physico-chemical bifunctional neural stem cells delivery system for spinal cord injury repair, Adv. Sci. 11 (21) (2024) e2308993.

[36] B. Shan, F. Wu, Hydrogel-based growth factor delivery platforms: strategies and recent advances, Adv. Mater. 36 (5) (2024) e2210707.

[37] P. Wu, C. Xu, X. Zou, K. Yang, Y. Xu, X. Li, X. Li, Z. Wang, Z. Luo, Capacitive-coupling-responsive hydrogel scaffolds offering wireless in situ electrical stimulation promotes nerve regeneration, Adv. Mater. 36 (14) (2024) e2310483.

[38] J. Yang, K. Yang, W. Man, J. Zheng, Z. Cao, C.Y. Yang, K. Kim, S. Yang, Z. Hou, G. Wang, X. Wang, 3D bio-printed living nerve-like fibers refine the ecological niche for long-distance spinal cord injury regeneration, Bioact. Mater. 25 (2023) 160–175.

[39] K.Y. Yang, J. Yang, W.T. Man, Z. Meng, C.Y. Yang, Z. Cao, J. Liu, K. Kim, Y.S. Liu, S.H. Yang, Y. Guo, Z.J. He, C. Ma, G.H. Wang, X.M. Wang, N-Cadherin-Functionalized nanofiber hydrogel facilitates spinal cord injury repair by building a favorable niche for neural stem cells, Adv. Fiber Mater. 5 (4) (2023) 1349–1366.

[40] Z. Chen, H. Zhang, C. Fan, Y. Zhuang, W. Yang, Y. Chen, H. Shen, Z. Xiao, Y. Zhao, X. Li, J. Dai, Adhesive, stretchable, and spatiotemporal delivery fibrous hydrogels harness endogenous neural stem/progenitor cells for spinal cord injury repair, ACS Nano 16 (2) (2022) 1986–1998.

[41] S. Ma, J. Zhou, T. Huang, Z. Zhang, Q. Xing, X. Zhou, K. Zhang, M. Yao, T. Cheng, X. Wang, X. Wen, F. Guan, Sodium alginate/collagen/stromal cell-derived factor-1 neural scaffold loaded with BMSCs promotes neurological function recovery after traumatic brain injury, Acta Biomater. 131 (2021) 185–197.

[42] X. Liu, M. Hao, Z. Chen, T. Zhang, J. Huang, J. Dai, Z. Zhang, 3D bioprinted neural tissue constructs for spinal cord injury repair, Biomaterials 272 (2021) 120771.

[43] W. Liu, Y. Luo, C. Ning, W. Zhang, Q. Zhang, H. Zou, C. Fu, Thermo-sensitive electroactive hydrogel combined with electrical stimulation for repair of spinal cord injury, J. Nanobiotechnol. 19 (1) (2021) 286.

[44] C. Zhang, D. Li, H. Hu, Z. Wang, J. An, Z. Gao, K. Zhang, X. Mei, C. Wu, H. Tian, Engineered extracellular vesicles derived from primary M2 macrophages with anti-inflammatory and neuroprotective properties for the treatment of spinal cord injury, J. Nanobiotechnol. 19 (1) (2021) 373.

[45] D. Ma, C. Fu, F. Li, R. Ruan, Y. Lin, X. Li, M. Li, J. Zhang, Functional biomaterials for modulating the dysfunctional pathological microenvironment of spinal cord injury, Bioact. Mater. 39 (2024) 521–543.

[46] C. Zhang, L. Xiang, J. Zhang, C. Liu, Z. Wang, H. Zeng, Z.K. Xu, Revisiting the adhesion mechanism of mussel-inspired chemistry, Chem. Sci. 13 (6) (2022) 1698–1705.

[47] H. Yan, Z. Wang, L. Li, X. Shi, E. Jia, Q. Ji, Y. Wang, Y. Ito, Y. Wei, P. Zhang, DOPA-derived electroactive copolymer and IGF-1 immobilized poly(lactic-co-glycolic acid)/hydroxyapatite biodegradable microspheres for synergistic bone repair, Chem. Eng. J. 416 (2021) 129129.

[48] C. Wang, Q. Zhang, G. Hou, C. Wang, H. Yan, Sustained release of EGF/bFGF growth factors achieved by mussel-inspired core-shell nanofibers with hemostatic and anti-inflammatory effects for promoting wound healing, Eur. Polym. 190 (2023) 112003.

[49] H. Yan, L. Li, X. Shi, J. Yeh, Y. Wei, P. Zhang, Conductive stretchable shape memory elastomers combining with electrical stimulation for synergistic osteogenic differentiation, Polym. Test. 90 (2020) 106672.

[50] D. Liu, G. Lu, B. Shi, H. Ni, J. Wang, Y. Qiu, L. Yang, Z. Zhu, X. Yi, X. Du, B. Shi, ROS-scavenging hydrogels synergize with neural stem cells to enhance spinal cord injury repair via regulating microenvironment and facilitating nerve regeneration, Adv. Healthcare Mater. 12 (18) (2023) e2300123.

[51] R. Guo, Q. Zhang, Y. Wu, H. Chen, Y. Liu, J. Wang, X. Duan, Q. Chen, Z. Ge, Y. Zhang, Extremely strong and tough biodegradable poly(urethane) elastomers with unprecedented crack tolerance via hierarchical hydrogen-bonding interactions, Adv. Mater. 35 (21) (2023) e2212130.

[52] R. Liu, H. Dai, Q. Zhou, Q. Zhang, P. Zhang, Synthesis and characterization of shape-memory poly carbonate urethane microspheres for future vascular embolization, J. Biomater. Sci. Polym. Ed. 27 (12) (2016) 1248–1261.

[53] P. Ping, W.S. Wang, X.S. Chen, X.B. Jing, The influence of hard-segments on two-phase structure and shape memory properties of PCL-based segmented polyurethanes, J. Polym. Sci. B Polym. Phys. 45 (5) (2007) 557–570.

[54] W. Fang, F. Sun, J. Tang, Q. Zhao, J. Chen, X. Lei, J. Zhang, Y. Zhang, Y. Zuo, J. Li, Y. Li, Porous electroactive and biodegradable polyurethane membrane through self-doping organogel, macromol, Rapid Commun. 42 (12) (2021) e2100125.

[55] H. Yan, L. Li, Y. Wang, J. Huang, Z. Wang, X. Shi, P. Zhang, An electrically and magnetically responsive nanocomposite of GdPO4·H2O/P3HT/PLGA with electrical stimulation for synergistically enhancing the proliferation and differentiation of pre-osteoblasts, New J. Chem. 43 (44) (2019) 17315–17326.

[56] M. Li, X. Li, Y. Lv, H. Yan, X.Y. Wang, J. He, C. Zhou, Y. Ouyang, Chiral MoS(2) @BC fibrous membranes selectively promote peripheral nerve regeneration, J. Nanobiotechnol. 22 (1) (2024) 337.

[57] K. Liu, S. Yan, Y. Liu, J. Liu, R. Li, L. Zhao, B. Liu, Conductive and alignment-optimized porous fiber conduits with electrical stimulation for peripheral nerve regeneration, Mater. Today Bio 26 (2024) 101064.

[58] Y. Tang, Z. Xu, J. Tang, Y. Xu, Z. Li, W. Wang, L. Wu, K. Xi, Y. Gu, L. Chen, Architecture-engineered electrospinning cascade regulates spinal microenvironment to promote nerve regeneration, Adv. Healthcare Mater. 12 (12) (2023) e2202658.

[59] Q. Wu, A. Razzak, H. Deng, H. Bai, J. Zhu, Mussel-inspired ferric ion-polydopamine complex as a facile, green and efficient platform to functionalize carbon fiber for improving interfacial adhesion of composites, Surface. Interfac. 37 (2023) 102742.

[60] Y. Ma, H. Shi, Q. Wei, Q. Deng, J. Sun, Z. Liu, B. Lai, G. Li, Y. Ding, W. Niu, Y. Zeng, X. Zeng, Developing a mechanically matched decellularized spinal cord scaffold for the in situ matrix-based neural repair of spinal cord injury, Biomaterials 279 (2021) 121192.

[61] A. Karimi, A. Shojaei, P. Tehrani, Mechanical properties of the human spinal cord under the compressive loading, J. Chem. Neuroanat. 86 (2017) 15–18.

[62] L.E. Bilston, L.E. Thibault, The mechanical properties of the human cervical spinal cord in vitro, Ann. Biomed. Eng. 24 (1) (1996) 67–74.

[63] Y. Li, L. Yang, Y. Hou, Z. Zhang, M. Chen, M. Wang, J. Liu, J. Wang, Z. Zhao, C. Xie, X. Lu, Polydopamine-mediated graphene oxide and nanohydroxyapatite-incorporated conductive scaffold with an immunomodulatory ability accelerates periodontal bone regeneration in diabetes, Bioact. Mater. 18 (2022) 213–227.

[64] L. Fan, C. Liu, X. Chen, L. Zheng, Y. Zou, H. Wen, P. Guan, F. Lu, Y. Luo, G. Tan, P. Yu, D. Chen, C. Deng, Y. Sun, L. Zhou, C. Ning, Exosomes-Loaded electroconductive hydrogel synergistically promotes tissue repair after spinal cord injury via immunoregulation and enhancement of myelinated axon growth, Adv. Sci. 9 (13) (2022) e2105586.

[65] J. Zheng, T. Chen, K. Wang, C. Peng, M. Zhao, Q. Xie, B. Li, H. Lin, Z. Zhao, Z. Ji, B. Z. Tang, Y. Liao, Engineered multifunctional zinc-organic framework-based aggregation-induced emission nanozyme for accelerating spinal cord injury recovery, ACS Nano 18 (3) (2024) 2355–2369.

[66] R. Hua, C. Zhao, Z. Xu, D. Liu, W. Shen, W. Yuan, Y. Li, J. Ma, Z. Wang, S. Feng, ROS-responsive nanoparticle delivery of ferroptosis inhibitor prodrug to facilitate mesenchymal stem cell-mediated spinal cord injury repair, Bioact. Mater. 38 (2024) 438–454.

[67] X. Gao, Z. Han, C. Huang, H. Lei, G. Li, L. Chen, D. Feng, Z. Zhou, Q. Shi, L. Cheng, X. Zhou, An anti-inflammatory and neuroprotective biomimetic nanoplatform for repairing spinal cord injury, Bioact. Mater. 18 (2022) 569–582.

[68] J. Li, J. Tian, C. Li, L. Chen, Y. Zhao, A hydrogel spinal dural patch with potential anti-inflammatory, pain relieving and antibacterial effects, Bioact. Mater. 14 (2022) 389–401.

[69] Y. Yang, J. Wang, S. Huang, M. Li, J. Chen, D. Pei, Z. Tang, B. Guo, Bacteria-responsive programmed self-activating antibacterial hydrogel to remodel regeneration microenvironment for infected wound healing, Natl. Sci. Rev. 11 (4) (2024) nwae044.

[70] X. Qian, T. Lu, C. Huang, D. Zheng, G. Gong, X. Chu, X. Wang, H. Lai, L. Ma, L. Jiang, X. Sun, X. Ji, M. Li, Y. Zhang, Bioinspired sonodynamic nano spray accelerates infected wound healing via targeting and disturbing bacterial metabolism, Adv. Funct. Mater. 34 (28) (2024) 2315576.

[71] H. Yan, C. Wang, Q. Zhang, P. Yu, Y. Xiao, C. Wang, P. Zhang, G. Hou, Conductive polyaniline particles regulating in vitro hydrolytic degradation and erosion of hydroxyapatite/poly(lactide-co-glycolide) porous scaffolds for bone tissue engineering, ACS Biomater. Sci. Eng. 9 (3) (2023) 1541–1557.

[72] W. Tan, T. Long, Y. Wan, B. Li, Z. Xu, L. Zhao, C. Mu, L. Ge, D. Li, Dual-drug loaded polysaccharide-based self-healing hydrogels with multifunctionality for promoting diabetic wound healing, Carbohydr. Polym. 312 (2023) 120824.

[73] R. Wang, X. Wu, Z. Tian, T. Hu, C. Cai, G. Wu, G. Jiang, B. Liu, Sustained release of hydrogen sulfide from anisotropic ferrofluid hydrogel for the repair of spinal cord injury, Bioact. Mater. 23 (2023) 118–128.

[74] Y. Wan, Y. Lin, X. Tan, L. Gong, F. Lei, C. Wang, X. Sun, X. Du, Z. Zhang, J. Jiang, Z. Liu, J. Wang, X. Zhou, S. Wang, X. Zhou, P. Jing, Z. Zhong, Injectable hydrogel to deliver bone mesenchymal stem cells preloaded with azithromycin to promote spinal cord repair, ACS Nano 18 (12) (2024) 8934–8951.

[75] X. Xue, X. Wu, Y. Fan, S. Han, H. Zhang, Y. Sun, Y. Yin, M. Yin, B. Chen, Z. Sun, S. Zhao, Q. Zhang, W. Liu, J. Zhang, J. Li, Y. Shi, Z. Xiao, J. Dai, Y. Zhao, Heterogeneous fibroblasts contribute to fibrotic scar formation after spinal cord injury in mice and monkeys, Nat. Commun. 15 (1) (2024) 6321.

[76] W. Li, L. Yu, J. Chi, J. Wang, Y. Liu, C. Wang, M. Zhang, G. Hou, Discovery of anti-inflammatory agents from 3, 4-dihydronaphthalene-1(2H)-one derivatives by inhibiting NLRP3 inflammasome activation, Eur. J. Med. Chem. 268 (2024) 116284.

[77] Y. Huang, M. Song, X. Li, Y. Du, Z. Gao, Y.Q. Zhao, C. Li, H. Yan, X. Mo, C. Wang, G. Hou, X. Xie, Temperature-responsive self-contraction nanofiber/hydrogel composite dressing facilitates the healing of diabetic-infected wounds, Mater. Today Bio 28 (2024) 101214.

[78] F. Wei, T. Wang, C. Wang, Z. Zhang, J. Zhao, W. Heng, Z. Tang, M. Du, X. Yan, X. Li, Z. Guo, J. Qian, C. Zhou, Cytoplasmic escape of mitochondrial DNA mediated by Mfn2 downregulation promotes microglial activation via cGas-sting Axis in spinal cord injury, Adv. Sci. 11 (4) (2024) e2305442.

[79] L. Zhang, C. Fan, W. Hao, Y. Zhuang, X. Liu, Y. Zhao, B. Chen, Z. Xiao, Y. Chen, J. Dai, NSCs migration promoted and drug delivered exosomes-collagen scaffold via a bio-specific peptide for one-step spinal cord injury repair, Adv. Healthcare Mater. 10 (8) (2021) e2001896.

[80] L. Luo, Y. Li, Z. Bao, D. Zhu, G. Chen, W. Li, Y. Xiao, Z. Wang, Y. Zhang, H. Liu, Y. Chen, Y. Liao, K. Cheng, Z. Li, Pericardial delivery of SDF-1α puerarin hydrogel promotes heart repair and electrical coupling, Adv. Mater. 36 (1) (2024) e2302686.

[81] M. Lian, Z. Qiao, S. Qiao, X. Zhang, J. Lin, R. Xu, N. Zhu, T. Tang, Z. Huang, W. Jiang, J. Shi, Y. Hao, H. Lai, K. Dai, Nerve growth factor-preconditioned mesenchymal stem cell-derived exosome-functionalized 3D-printed hierarchical porous scaffolds with neuro-promotive properties for enhancing innervated bone regeneration, ACS Nano 18 (10) (2024) 7504–7520.

[82] J. Ma, J. Li, X. Wang, M. Li, W. Teng, Z. Tao, J. Xie, Y. Ma, Q. Shi, B. Li, Saijilafu, GDNF-loaded polydopamine nanoparticles-based anisotropic scaffolds promote spinal cord repair by modulating inhibitory microenvironment, Adv. Healthcare Mater. 12 (8) (2023) e2202377.

[83] V. Veneruso, E. Petillo, F. Pizzetti, A. Orro, D. Comolli, M. De Paola, A. Verrillo, A. Baggiolini, S. Votano, F. Castiglione, M. Sponchioni, G. Forloni, F. Rossi, P. Veglianese, Synergistic pharmacological therapy to modulate glial cells in spinal cord injury, Adv. Mater. 36 (3) (2024) e2307747.

[84] X.T. He, X. Li, M. Zhang, B.M. Tian, L.J. Sun, C.S. Bi, D.K. Deng, H. Zhou, H.L. Qu, C. Wu, F.M. Chen, Role of molybdenum in material immunomodulation and periodontal wound healing: targeting immunometabolism and mitochondrial function for macrophage modulation, Biomaterials 283 (2022) 121439.

[85] X. Huang, L. Zheng, Y. Zhou, S. Hu, W. Ning, S. Li, Z. Lin, S. Huang, Controllable adaptive molybdate-oligosaccharide nanoparticles regulate M2 macrophage mitochondrial function and promote angiogenesis via PI3K/HIF-1α/VEGF pathway to accelerate diabetic wound healing, Adv. Healthcare Mater. 13 (3) (2024) e2302256.

[86] P. Zhang, Z. Chen, D. Lu, Y. Wu, M. Fan, J. Qian, J. Ge, Overexpression of COX5A protects H9c2 cells against doxorubicin-induced cardiotoxicity, Biochem. Biophys. Res. Commun. 524 (1) (2020) 43–49.

[87] Y. Zhou, R. Wu, X. Wang, Y. Jiang, W. Xu, Y. Shao, C. Yue, W. Shi, H. Jin, T. Ge, X. Bao, C. Lu, Activation of UQCRC2-dependent mitophagy by tetramethylpyrazine inhibits MLKL-mediated hepatocyte necroptosis in alcoholic liver disease, Free Radical Biol. Med. 179 (2022) 301–316.

[88] K. McIntosh, Y.H. Khalaf, R. Craig, C. West, A. McCulloch, A. Waghmare, C. Lawson, E.Y.W. Chan, S. Mackay, A. Paul, R. Plevin, IL-1β stimulates a novel, IKKα -dependent, NIK -independent activation of non-canonical NFκB signalling, Cell. Signal. 107 (2023) 110684.

[89] Y. Lan, T. Yang, Q. Yue, Z. Wang, X. Zhong, X. Luo, B. Zuo, M. Zhang, T. Zeng, B. Liu, H. Guo, IRP1 mediated ferroptosis reverses temozolomide resistance in glioblastoma via affecting LCN2/FPN1 signaling axis depended on NFKB2, iScience 26 (8) (2023) 107377.

[90] Z. Sun, Y. Wang, X. Pang, X. Wang, H. Zeng, Mechanisms of polydatin against spinal cord ischemia-reperfusion injury based on network pharmacology, molecular docking and molecular dynamics simulation, Bioorg. Chem. 140 (2023) 106840.